Notice

This is a non-peer reviewed preprint submitted to Essoar. This manuscript has been submitted to Geophysical Journal International on 24-07-2022 with reference number GJI-22-0610 (Status: In Revision). Please check for the most recent version before referencing or citing since subsequent revised versions may differ in text and content.

Details

Role of fluid on earthquake occurrence: Example of the 2019 Ridgecrest and the 1997, 2009 and 2016 Central Apennines sequences

Author

Kariche, Jugurtha**;** USTHB, Dept. of Geophysics, FSTGAT, Algiers, Algeria, Institut de Physique du Globe, CNRS-UMR751**6**, EOST - Strasbourg, F-´ 67084, France.

Contact: jkariche@gmail.com

Or by twitter: https://twitter.com/JkaricheKariche

Role of fluid on earthquake occurrence: Example of the 2019 Ridgecrest and the 1997, 2009 and 2016 Central Apennines sequences

Jugurtha Kariche[1,2]

[1] USTHB, Laboratoire de Géophysique, FSTGAT, Algiers, Algeria.

[2] Institut Terre et Environnement de Strasbourg (ITES), CNRS-UMR7063.

[*]Corresponding author: Jugurtha Kariche (jkariche@gmail.com)

July 2022

SUMMARY

This paper focuses on the study of the temporal evolution of seismicity and the role of fluids during major earthquake sequences that occurred in the central Apennines and Southern Walker Lane belt-Eastern California Shear Zone over the last two decades: The 1997 Colfiorito sequence, the 2009 L'Aquila sequence, the 2016 Amatrice-Norcia sequence, and the 2019 Ridgecrest sequence. The availability of different high-quality seismic catalogs offers the opportunity to evaluate in detail the temporal evolution of the earthquake's size distribution (or b-value) and propose a physical explanation based on the effect of the fluid flow process in triggering seismicity. For all seismic sequences, the b-value time series show a gradual decrease from a few months to one year before mainshocks. The gradual decrease in the b-value is interpreted in terms of coupled fluid-stress intensity as a gradual increase in earthquake activity due essentially to the short-term to intermediate-term pore-fluid fluctuations. For the 2016 Amatrice-Norcia sequence and the 2019 Ridgecrest sequence, the temporal variation of the b-value during the foreshock sequence is characterized by a double b-value minimum separated by a short-lived b-value increase as observed in laboratory experiments on water-saturated rocks. Based on laboratory experiment results, the observed short–term fluctuation of the b-value is presented here as an accelerating crack growth due essentially to the fluid flow instability. Despite that the occurrence of seismic precursors could have been predictable in areas with high dense seismic networks, the different b-value time series show difficulty to establish a correspondence between the duration of the foreshock activity and the magnitude of the next largest expected earthquake. This may suggest that the spatial and temporal evolution of fluid migration controls the size of the ruptures.

47   **INTRODUCTION**

48   Several studies have suggested a relation between the occurrence of earthquake sequences

49   and the temporal change in the relative size distribution of earthquakes quantified by the

50   Gutenberg-Richter (GR) b-value (Berg, 1968; Scholz, 1968; Smith, 1981; Wiemer & Wyss,

51   2000…). The analyzes of a series of 60 foreshocks and 428 aftershocks related to three

52   moderate earthquakes occurred on the Fairbank region of Alaska shows that the Gutenberg-

53   Richter (GR) b-value was abnormally low (between 0.34 to 0.45) before large events and was

54   restored taking a typical value of 0.85 to 0.95 during and after each mainshocks (Berg, 1968).

55   The seismicity analysis of the 1967 Caracas (Mw 6.7) earthquake sequence, the 1971 San

56   Fernando (Mw 6.4) earthquake sequence, and the 1968-1978 New Zealand earthquake

57   sequence reveal that the temporal variation in the b-value was remarkably coupled with the size

58   of moderate to strong earthquakes. A large time scale decrease in the b-value associated with

59   an acceleration of aseismic slip is observed before the Mw 8.1 Iquique, Chile and the Mw 9.0

60   Tohoku-Oki earthquakes (Nanjo et al., 2012; Scholz, 2019). Several studies argues that the

61   acceleration of aseismic slip is favored by a variation of pore fluid pressure at depth (Segall &

62   Rice, 1995; Ruhl et al., 2016;Cappa et al., 2019 ; De Barros et al., 2020). The gradual decrease

63   in the b-value on a much shorter time scale is also observed in the four-month-long foreshock

64   sequence preceding the 2009 L'Aquila earthquake (Gulia et al., 2016). The temporal variation

65   of the b-value before L'Aquila mainshock correlate with the change of Vp/Vs from January to

66   the April 6 (Lucente et al., 2010). The simulateous change in b-value and Vp/Vs in the case of

67   the L'Aquila sequence may interpret as a nucleation process due to an overpressurised volume

68   controlled by fluid migration at depth (Chiaraluce, 2012).

69   The comparison between the temporal evolution of b-value and the effective normal stress

70   in California show a decrease in the b-value associated with a decrease in effective normal

71   stressing rate (Khoshmanesh & Shirzaei.,2018). The maximum increase in the Coulomb stress

72 rate (up to 0.45 bar/yr spanning the period from 2003 to 2010) along the central part of the San

73 Andreas Fault system also coincides with the decrease in effective normal stress caused by the

74 evolution of pore-fluid pressure at depth (Khoshmanesh & Shirzaei.,2018). These results argue

75 that a strong correlation exists between the fluid migration and the temporal evolution of the b-

76 value along the central part of the San Andreas fault. In the Southern Walker Lane belt (SWL)-

77 Eastern California Shear Zone (ECSZ), high-resolution optical satellite imagery analysis

78 reveals a considerable contribution of the inelastic processes to the total diffuse deformation

79 following the 2019 Ridgecrest earthquake sequence (Antoine et al., 2021). The high Vp/Vs

80 ratio covering the complex fault zones of the 2019 Ridgecrest foreshock-mainshock sequence

81 (Tong et al., 2021) denotes that the change in the pore-fluid pressure near the Ridgecrest fault

82 zone may be considered as one of the plausible mechanisms explaining the diffuse inelastic

83 deformation observed during the 2019 Ridgecrest sequence. A stress changes modeling results

84 taking onto account the variation in the Vp/Vs ratio due to the diffusive effect of fluids during

85 the Mw6.4 Ridgecrest foreshock reveals that the value of fluid diffusivity necessary to trigger

86 the next Mw7.1 mainshock is estimated to $\leq 2.32\ 10^4\ cm^2/s$ (Kariche, 2022). This value seems

87 to be low compared with the value obtained by Hudnut et al., (1989) for the 1987 Superstition

88 Hills sequence and may explain the difference in the time delay between mainshocks in relation

89 with to the two sequences.

90 A laboratory fracturing experiment on fluid-saturated rocks also predicts a variation in the

91 Vp/Vs due to the change in the rheological properties of the seismogenic crust following large

92 earthquakes. Fracture mechanics modeling and laboratory experiments for dry and water-

93 saturated specimens shows that the gradual decrease in the b-value related to a progressive

94 increase in acoustic emission rate (AE) is only visible in water-saturated rocks (Main et al.

95 1990). Laboratory experiments at constant pore-fluid volume predict a fluctuation in the b-value

96 before major cracks and argue the idea that the fluid affects considerably the size and the

97   distribution of future cracks (Sammonds et al., 1992). Other strong correlations between b-value

98   and fluid migration are also found in a crustal range of the Taiwan orogenic belt (Chen et al.,

99   2019).

100   In this paper, I explore the influence of fluids migration on earthquake occurrence by analyzing

101   the temporal evolution of seismicity for two tectonically active zones with available high-

102   quality dense seismic networks: the Central Apennine (Italy) and the SWL-ECSZ. Several

103   major seismic sequences are studied in details: the 1997 Colfiorito, the 2009 l'Aquila and the

104   2016 Amatrice-Norcia for the Central Apennine seismic zone and the 2019 Ridgecrest (CA)

105   sequence for the SWL-ECSZ. These sequences are explored in terms of seismic productivity

106   and related fluid migration. By analyzing the evolution of seismicity and stress redistribution,

107   I found a causative relation between the pore fluid effect and the Spatio-temporal evolution of

108   crack growth before and during major earthquakes. The results are also compared to the

109   laboratory experiments for a better constrain of the role of fluids in the different phases of the

110   earthquake generation.

111   **METHODOLOGY**

112   **1. G-R b-value time series modeling**

113   A first empirical relation between the frequencies and magnitudes of earthquakes is proposed

114   by Gutenberg & Richter (1950):

$$Log_{10}[N(M)] = a - bM \qquad (1)$$

116   Where *a* and *b* are the G-R constants, *M* is the magnitude, and *N(M)* is the number of

117   earthquakes in a specific time window of events with a magnitude range between *M* and $\pm \delta M$.

118   The b-value for an entire catalog is estimated by the maximum likelihood value (Aki, 1965):

119
$$b = \frac{1}{ln(10)(\overline{M} - M_c)} \qquad (2)$$

120 Where $\overline{M}$ represents an average magnitude value for a population of earthquakes satisfying the

121 condition $M \geq M_c$, and M_c is the magnitude of completeness defined as the lowest magnitude

122 at which all the events in a space-time volume are detected (Wiemer & Wyss, 2000; Woessner

123 & Wiemer, 2005).

124 The b-value time series can be rewritten as (Woessner & Wiemer, 2005):

125
$$b = \frac{Log_{10}(e)}{\left[\langle M \rangle - \left(M_c - \Delta M_{bin}/2\right)\right]} \qquad (3)$$

126 Where $\langle M \rangle$ represents the mean magnitude of the sample and ΔM_{bin} is the binning width of the

127 catalogue (Aki, 1965).

128 The standard deviation of b-value can be obtained using the Shi & Bolt (1982) approach:

129
$$\delta b = 2.3 \, b^2 \sqrt{\frac{\sum_i(M_i \, \{M\})}{n \, (n-1)}}$$

130 Where *n* is the sample size.

131   In order to evaluate the temporal variation of crack distribution on a seismogenic volume,

132 the temporal variation in b-value is computed using the 3D frequency–magnitude approach of

133 Wyss *et al.* (1998) with an appropriate time window. The b-value time series computation

134 procedure used in this study and based on the fixed number of events technics is in general

135 similar to those used by Gulia & Wiemer, (2019) or Dascher-Cousineau et al., (2020) which

136 take into account the space-time evolution of Mc in the b-value estimation. The determination

137 of Mc is based on the assumption that the seismic events are self-similar (Wiemer & Wyss,

138 2000). The most robust way to deal with the dependence of the b-value time series on Mc is to

139   choose a large value of Mc for the entire time series catalog, but this approach led to maximizing

140   uncertainties when the computation of the b-value is made for a smaller number of earthquakes

141   sample.

142   The correct assessment of the completeness magnitude Mc for each earthquake sample

143   used here is made according to the automatic correction of the completeness level of Mc through

144   time using the Maximum curvature method (MAXC) (Wiemer & Wyss, 2000). The Mc and the

145   b-value are performed simultaneously by computing the maximum value of the first derivate of

146   the frequency-magnitude plot. The MAXC technique provides a reasonable resolution of the b-

147   value over time and tends to minimize uncertainties due to smaller sample sizes compared with

148   the b-value estimates using fixed Mc-approaches. In order to completely leave the

149   underestimation of the Mc value over time, a value of 0.2-to 0.5 is added to the Mc-values by

150   taking into account the fact that the overall shape of the time series is invariant for at least Mc

151   ranges associated with each earthquake sequence.

152   For the 2019 Ridgecrest sequence, I use the highest confidence QTM seismicity catalog

153   for Southern California (Ross *et al.* 2019)spanning the period from 2000 to 2018 and the USGS-

154   NEIC updated high-resolution catalog for the period between March 2018 to March 2020

155   combined with the Shelly (2020) higher-resolution Ridgecrest datasets. For 1997, 2009, and

156   2016 Central Apennine sequences, I use the entire seismic catalog of the Istituto Nazionale Di

157   Geofisica E Vulcanology covering the period between 1985 and 2018 combined with the

158   catalog for the same region published by Gasperini *et al.* (2013) augmented by the recent high-

159   resolution catalog of Tan et al. (2021) in relation with the 2016-2017 Amatrice-Norcia

160   sequence.

161   **2. Fluid flow and the evolution of seismicity**

162   Taking into account the complexity of the earthquake generation, a realistic representation

163   of the temporal evolution of seismicity following a seismic event can be expressed as (Utsu

164   1969; Utsu & Ogata 1995):

$$\frac{dN(t)}{dt} \propto \frac{k}{(c+t)^p} \qquad (4)$$

166   Where $\frac{dN(t)}{dt}$ represents the aftershock frequency, t is the time from the main shock triggered

167   event, k is the productivity of aftershocks that depends on the total number of events, p is the

168   power law exponent and c define the time delay before the onset of the power-law aftershock

169   decay rate and depends on the rate of activity in the earlier part of the seismic sequence. The

170   value of c is also related to the incompleteness of seismic catalogs after strong earthquakes.

171   Guo & Ogata (1997) obtained a ranges of c values between 0.003d and 0.3d for various

172   earthquake datasets. In our simulation, the c value is fixed as 0.01d. This value of c is selected

173   to be the lowest possible in order to obtain sufficient aftershocks productivity in the very early

174   part of the aftershock sequence (Enescu et al., 2007; Kariche et al., 2018).

175   Based on the Nur and Booker (1972) hypothesis, the aftershock frequency within a seismogenic

176   volume can be proportional to the temporal evolution of pore-fluid pressure as:

$$\frac{dN}{dt} = \frac{1}{\alpha} \int \frac{\partial P}{\partial t} \, dv \qquad (5)$$

178   Where α is a constant that defines the pore-fluid pressure increase with a cracks evolution in

179   appropriate volume v. P represents the pore-fluid pressure variation following an earthquake.

180   Taking into account the boundary conditions for a steady state source and if we suppose a linear

181   fluid-flow process, a simple poroleastic solution is given by Malagnini *et al*. (2012):

182
$$P(x,t) = (P_0 - P_1)erfc\left(\frac{x}{2\sqrt{ct}}\right) + P_1 \qquad (6)$$

183 Where c represents the value of fluid diffusivity and $erfc$ is the complementary error function.

184 For nucleation assisted by fluids, Abramowitz & Stegun (1970) wrote the $erfc$ function as:

185
$$erfc\left(\frac{x}{2\sqrt{ct}}\right) = \frac{2}{\sqrt{\pi}} \int_{\frac{x}{2\sqrt{ct}}}^{\infty} e^{-\xi^2} d\xi \qquad (7)$$

186 In this case, the initial and boundary conditions may be posed as:

187
$$\begin{cases} P(x = 0, t > 0) = P_0 = \lambda_f \, \rho_r \, gz \\ P(x > 0, t = 0) = P_1 = \rho_w gz \end{cases}$$

188 Where ρ_r and ρ_w are respectively the rocks and fluid density, λ_f is the pore fluid pressure

189 coefficient for an arbitrary depth and range between 0.6 and 0.8 for fault reactivation assisted

190 by fluid (Rikitake 1972).

191 Replacing the 1 D pore fluid pressure form on the Nur & Booker (1972) equation with choosing

192 the complementary error as expressed by Abramowitz & Stegun (1970), a complete aftershocks

193 pore-fluid diffusion solution may be written as:

194
$$\frac{dN}{dt} = \frac{1}{\alpha} \frac{(P_0 - P_1)}{2\sqrt{\pi ct^3}} \int_0^{\infty} x \, e^{\left(-\frac{x^2}{4ct}\right)} dx = \frac{(P_0 - P_1)\sqrt{c}}{\alpha\sqrt{\pi}} \frac{1}{\sqrt{t}} \qquad (8)$$

195 This equation shows that in the presence fluid, the aftershocks decay is proportional to $\frac{1}{\sqrt{t}}$.

196 However, if an external source does not provide a sufficient fluid volume, the transient signal

197 will decrease and a permanent Omori type signal (1/t) will appear.

198 **THE CENTRAL APENNINE SEQUENCE**

199 The 1997, 2009 and 2016 Central Apennine earthquake sequences start with the 1997

200 Colfiorito (Umbria-Marche) sequence which struck the northern part of the Appenine in Italy

201   (Amato et al., 1998; Stramondo et al., 1999; Deschamps et al., 2000; Chiaraluce et al., 2003…).

202   The Colfiorito sequence is characterized by six earthquakes with magnitude larger than 5.0 and

203   two earthquakes with magnitude larger than 5.7 (Figure 1, Figure 2A & S2). The first

204   earthquake occurred on September 26 at 00:33 UTC with a magnitude Mw =5.7. Nine hours

205   later, another strong earthquake with Mw 6.0 struck the Colfiorito region with a 3 km distance

206   from the first event (Amato et al., 1998). The Mw 5.7 event is considered as a foreshock

207   preceding the Mw 6.0 mainshock (Amato et al., 1998). The hypocentral depth for the two events

208   is approximatively equal and situated around 4 to 5 km depth (Figure 1, Figure 2A & Figure

209   S2). The third event with a magnitude Mw =5.9 triggers 18 days after at 12 km south east of

210   the first event (Figure S2). The analysis of the spatial and temporal evolution of seismicity

211   related to the 1997 Colfiorito shows that the seismicity is mainly controlled by the poroelastic

212   properties of the seismogenic zone and fluid low (Antonioli *et al.* 2005). Using the fluid

213   triggering hypothesis, the value of fluid diffusivity able to trigger a 1997 Colfiorito sequence

214   range is estimated between 2.2 x 10^5 and 9.0 x 10^5 cm^2/s (Antonioli *et al.* 2005).

215   On April 6, 2009 at 01h32 GMT, a devastating earthquake with a magnitude Mw 6.3

216   occurred on normal fault at intramontane basin near the city of L'Aquila (Figure 1). This

217   sequence began with a series of foreshocks six months prior the mainshock in a ~4 km long

218   band on the L'Aquila fault zone (Figure 2B; Figure S3). The near field seismic wave analysis

219   shows that the Spatio-temporal evolution of foreshocks correlates with a clear variation in

220   seismic wave properties at depth (Lucente *et al.* (2010). The Vp/Vs value rose from 1.85 to

221   more than 1.92 near the epicenter area of the 2009 L'Aquila earthquake a week before the

222   mainshock and decreased down to 1.85 a few hours before (Lucente *et al.,* 2010). According to

223   the dilatancy-diffusion hypothesis (Nur, 1972; Scholz et al., 1973), the change in Vp/Vs near

224   L'Aquila is interpreted as the variation in elastic properties of the medium due to the fluid

225   migration along the L'Aquila fault zone (Lucente *et al.,* 2010; Chiaraluce, 2012; Scholz, 2019).

226 Based on the temporal change in the Vp/Vs ratio, the triggering mechanism related to the

227 L'Aquila earthquake is resolved as a mechanism governed by the presence of a deep large fluid

228 reservoir (Lucente et al. 2010). Indeed, the complexity of the fault zone, the deep thrust fault,

229 and the low angle active normal faults observed nearby the L'Aquila major rupture (Chiodini

230 et al., 2004) may be interpreted as a structural seal that favors the fluid accumulation and creates

231 an overpressurized volume near the L'Aquila hypocentral depth.

232
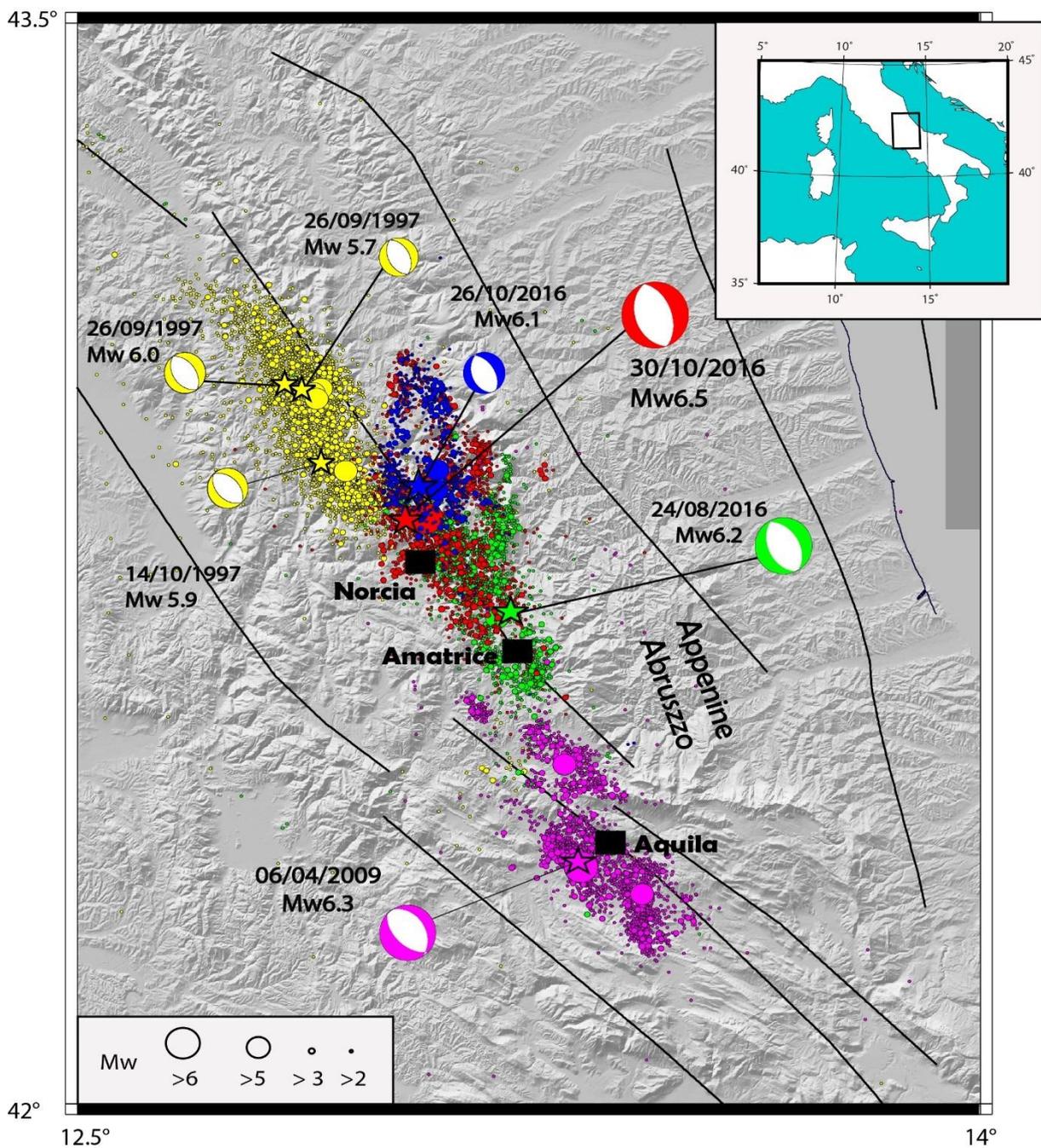
233 **Figure 1:** *Seismicity and focal mechanisms of major earthquakes occurred in the central*

234 *Apennines (Italy) spanning the period from 1997 to 2016. Each earthquake sequence with a*

235 *related mainshock focal mechanism is represented by specified color. For example, the*

236 *magenta color represents the spatial distribution of the events associated with the 2009*

237 *L'Aquila earthquake sequence, the focal mechanism associated to the L'Aquila mainshock is*

238 *also represented by the same color. The focal solutions are from the Global Centroid Moment*

239 *Tensor (https://www.globalcmt.org/CMTsearch.html). The seismicity of the Central Apennine*

240 *is from INGV (http://terremoti.ingv.it/en). The inset figure represents the location of the studied*

241 *area. Note that the 2016 Amatrice-Norcia seismic sequence may view as a unique earthquake*

242 *swarm divided into three smaller sequences. The colored data (green, blue, red) mimic the*

243 *seismic migration from the August 24th (sequence in green), and culminating with the October*

244 *30th, Mw 6.5 earthquake (sequence in red).*

245

246   From the structural point of view, the evolution of fault geometry near the L'Aquila fault

247 zone seems to be controlled by a set of conjugate EW-NS faults system in a transtentional

248 regime at the limit of large active fault segments. The aftershock distribution analysis following

249 the 2009 L'Aquila mainshock shows that a non-neglected part of the aftershock productivity (~

250 32% of the total aftershocks recorded during the period from April to December 2009) is located

251 at the limit of the fault slip zone. Scholz (2019) interprets this spatial distribution of the

252 aftershocks as typical for a triggering mechanism assisted by a poroelastic and/or viscoelastic

253 stress relaxation.

254   After the 2009 L'Aquila earthquake, the Central Apennine was followed by three moderate

255 earthquakes with a magnitude M≥ 6.0: the 2016 August 24 Amatrice earthquake (Mw 6.2), the

256 2016 August 26 Ussita earthquake (Mw 6.1) and the 2016 October 30 Norcia earthquake (Mw

257   6.5). Thus, these three sequences fill the gap between the Colfiorito and L'Aquila earthquake

258   series (Figure1). Focal mechanism of the three earthquakes shows a normal faulting solution

259   (Figure1) consistent with a rate of 3-4 mm/yr in Apennines zones. The mechanics of

260   deformation in the Central Appenines is complex. The strain release nearby Amatrice fault-

261   zone is accommodate by a complex interaction between the main normal faults and a secondary

262   structures inherited from the pre-Quaternary compressional tectonic phases (Cheloni *et*

263   *al.*,2017). Pino *et al.* (2019) point out that the seismic sequences starting with the Amatrice and

264   after Ussita earthquakes advance the triggering of the October 30 Norcia earthquake (Mw 6.5).

265   Based on the fact that the earthquake triggering mechanism is assisted by fluids, Pino *et al.*

266   (2019) obtain an average value of fluid diffusivity able to trigger the 2016 Amatrice-Norcia

267   sequence equal to $1.5 \ 10^4 \ cm^2/s$. The values are low compared to the values obtained for the

268   1997 Colfiorito sequence (Antonioli *et al.*, 2005) and may explain the variability in earthquake

269   time delay (from hours to days) between the two sequences (Figure 2A & C). In the case of the

270   1997 Colfiorito and the 2016 Amatrice-Norcia sequences, the difference in fluid characteristics

271   obtained by different authors (Antonioli *et al.* 2005; Pino *et al.* 2019…) correlate with the

272   spatial variation of the seismicity from south to north in the Central Appenine fault zone

273   (Figure1). The spatial variation in fluid diffusivity also explains the high degree of

274   heterogeneity along the central Appenine fault-zone and the difference in time delay between
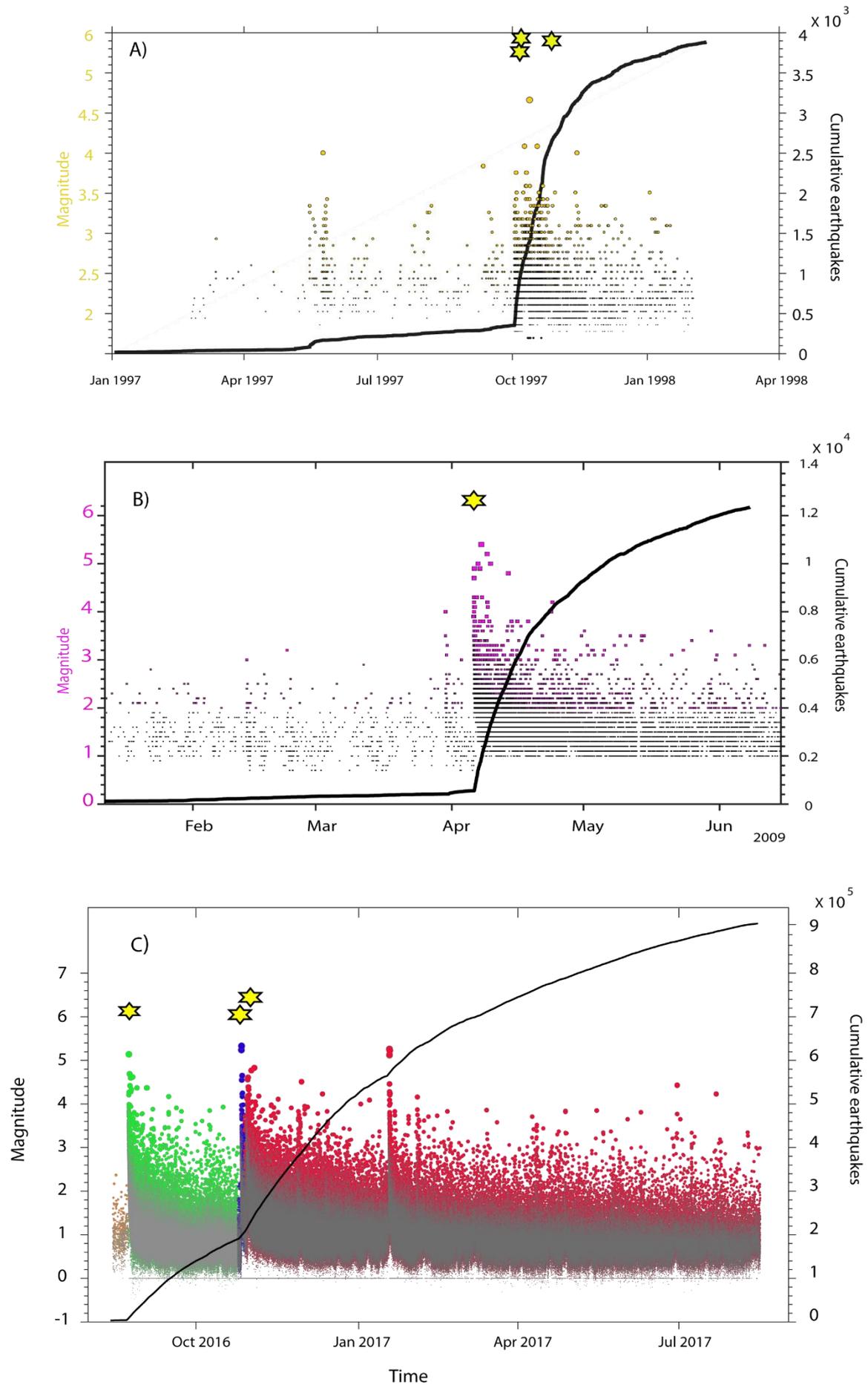
275   major earthquakes.

276

277

278

279

280

281

282 **Figure 2:** *Evolution of the Cumulative number of earthquakes and magnitude distribution*

283 *through time for: **A**) the 1997 Colfiorito sequence, **B**) the 2009 L'Aquila sequence and **C**) the*

284 *2016 Amatrice-Norcia sequence. The earthquakes datasets used for A) and B) are from INGV.*

285 *The earthquake database used for construct the C) plot is derived from a recent high precise*

286 *determination of ~900, 000 earthquakes derived from deep-neural-network-based picker (Tan*

287 *et a.,2021). The earthquake magnitude evolution in time from each sequence is represented by*

288 *a specific color same as in Figure 1. The yellow stars represent the major events for each*

289 *sequence. The Time evolution of earthquakes and related magnitude distribution are*

290 *constructed using the Zmap software (Wyss & Wiemer.,2000).*

291

292 **THE 2019 RIDGECREST SEQUENCE**

293 In July 2019, two moderates to strong earthquakes with a magnitude Mw 6.4 and 7.1 struck

294 Ridgecrest (California) in SWL-ECSZ region. Earthquake ruptures characteristics deduced

295 from InSAR, source time functions and early aftershock analysis indicate that the Mw 6.4 and

296 the Mw7.1 earthquakes occurred on conjugate strike-slip faults within a time interval

297 approximately equal to 34 hours at 12 km distance and 8 to 11 km depth, respectively (Figure

298 3; Barnhart *et al*. 2019; Fielding *et al.* 2020…). Early surface deformation analysis deduced

299 from Synthetic Aperture Radar Interferogram (InSAR) and focal mechanism analysis indicates

300 that the 2019-07-04 (Mw6.4) and the 2019-07-06 (Mw7.1) events occurred on NE-SW and

301 NW-SE trending conjugate strike-slip faults. The Ridgecrest fault zone is a part of the Indian

302 Wells Valley, which is connected to the Central Basin and Range tectonic province. This area

303 is bounded on the West by the Sierra Nevada Mountains, on the South by the Garlock fault, and

304 on the East by the Walker Lane belt (Figure 3). The Little Lake (or Ridgecrest) fault zone

305 (LLFZ) is defined as an important component of the SWL-ECSZ which accommodates a non-

306   neglected part of the Pacific-North America plate boundary displacement (Figure 3). The

307   seismotectonics of the Ridgecrest region reflects the complex interaction of left lateral and right

308   lateral conjugate strike slip faults in a variable tectonic regime (Figure 3). The transition from

309   transpressional regimes near LLFZ to transtensional regimes at the north of Ridgecrest (near

310   Coso-Range) agrees with the rotation of the maximum principal stress (Combs 1980) and may

311   be interpreted as a result of a large weakening mechanism of an immature faults.

312   Based on the poromechanical model proposed by Rice (1992), Axen (1992) interprets the

313   active deformation along the low angle normal fault in the Indian Wells Valley – Coso Range

314   as a consequence of a weakening mechanism due to abnormally elevated pore-fluid pressure in

315   both brittle and ductile regime. In this case, the permeability in active fault zone must be higher

316   than its surrounding rocks. Large volumes of fluid migrate from ductile to brittle zone in active

317   mylonite area are also observed in relation to the detachment zones in the Central Mojave Desert

318   (Axen 1992). The analysis of a high resolution imaging derived from satellite optical imagery

319   shows that the presence of inelastic failure related to the 2019 Ridgecrest earthquake sequence

320   reflects a mylonitic deformation of the fault damage zone (Barnhart *et al*.,2020). The observed

321   mylonitic zones are directly correlated to the degree of fault maturity of the Ridgecrest

322   conjugated ruptures. The analysis of Line of sight (LOS) interferometric Synthetic Aperture

323   Radar (SAR) displacements following the 2019 Ridgecrest sequence attests that a part of the

324   observed early 2019 Ridgecrest postseismic deformation is indicative of a poroelastic rebound

325   (Wang & Bürgmann., 2020). The LOS displacements derived from both Sentinel-1 and

326   COSMO-SkyMed (CSK) SAR data reveals that the maximum postseismic deformation along

327   the LOS of ascending satellite tracks is located at the northwest of the Mw 7.1 epicenter near

328   the Coso geothermal fault zone (Wang & Bürgmann, 2020). Most of the seismicity recorded

329   before the 2019 Ridgecrest sequence is relatively small (M ≤ 3). The largest event recorded in

330   SWL is the 1872 M7.5 Owens Valley earthquake (Figure S1; Monastero *et al.* 2002). The 1872

331 M7.5 Owens Valley earthquake is dominated by a right-lateral shearing deformation along the

332 Owens Valley fault (Figure S1). The recurrence of earthquake with a magnitude M ≥ 5.0 in

333 SWL is approximatively equal to 20 years with two significant sequences with four moderate

334 events (M ≥ 5.0) occurred near Ridgecrest city between 1995 and 1998 (Hauksson *et al.* 1995).

335 This recurrence pattern has been culminated by the occurrence of the 2019 Ridgecrest sequence

336 (Mw 6.4; Mw 7.1). The study of the mechanics of earthquake and fault interaction in the context

337 of conjugate strike-slip faults indicate a clear influence of fluid migration on the occurrence of

338 moderate to large earthquakes in the SWL tectonic domain (Kariche, 2022). Based on the

339 Coulomb poroelastic stress change modeling approach, the time delay between two conjugate

340 strike-slip earthquakes seems to be coupled to the variation in fluid diffusivity along

341 heterogeneous faults (Kariche, 2022). These observations are in concordance with the Cocco &

342 Rice (2002) Coulomb stress transfer modeling results taking into account the presence of high

343 pore fluid pressure at hypocentral depth.

344 Considering the ~34 hr characteristic time delay of the 2019 Ridgecrest sequence

345 representing the time delay between the Mw 6.4 foreshock and the Mw 7.1 mainshock (Kariche,

346 2022) and a fluid viscosity of 3×10^{-4} Pa.s, the average value of permeability necessary to trigger

347 the Mw7.1 Ridgecrest event is estimated between 10^{-14}-10^{-15} m^2. Despite the fact that this value

348 is higher than the value obtained by Cocco and Rice (2002) for normal fault geometries, it

349 seems to be in a good agreement with the permeability values obtained recently by Miller

350 (2020) for the 1992 Lander-Big Bear conjugated sequence and based entirely on the conceptual

351 model of permeability dynamics as proposed by the same author. Also, this permeability value

352 estimation seems to be in a good agreement with the value obtained by Nespoli *et al.* (2018) for

353 the 2012 Emilia-Romagna earthquake sequence. The temporal and spatial evolution of major

354 events following the Mw 6.4 foreshock sequence may explain the significant increase in the

355 value of permeability along cracks following the Mw7.1 earthquake. Based on this assumption,

356   the temporal distribution of earthquake frequency and related moment release must predict a

357   temporal fluctuation of the G-R b-value during the 2019 Ridgecrest sequence caused essentially

358   by the variation of pore-fluid pressure at depth.

359
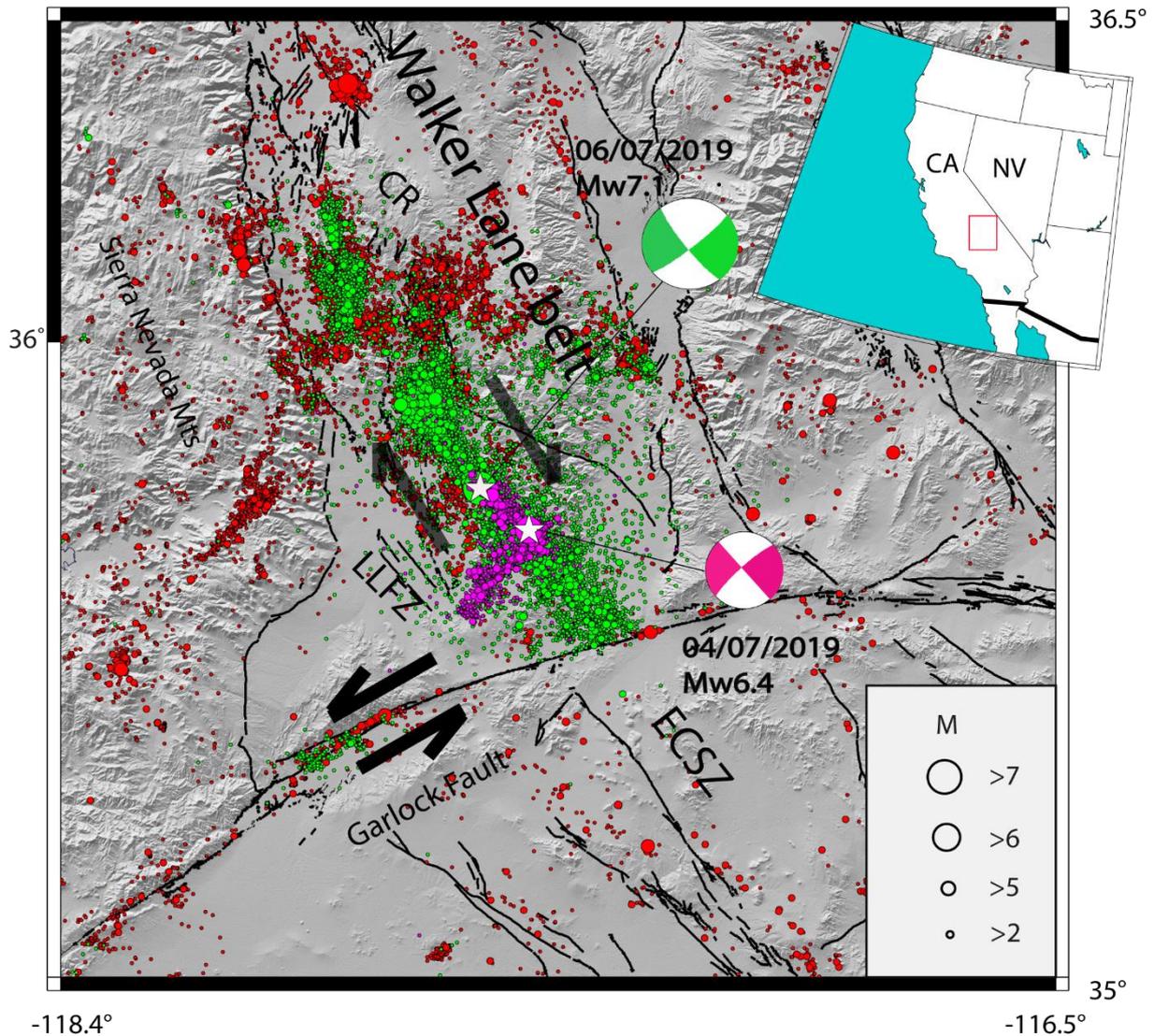
360   **Figure 3:** *Seismicity along the Southern Walker Lane (SWL)-Eastern California Shear zone*

361   *(ECSZ) from 2008 to 27/10/2019 using combined SCEDC QTM catalog (Ross et al. 2019) and*

362   *the high definition NEIC-USGS catalog (https://earthquake.usgs.gov/earthquakes/search/).*

363   *The color circles indicate the seismicity at different periods: red from the period between 1980*

364   *and July 2019; green for the period covering the 2019 Ridgecrest foreshock activity and*

365   *magenta for events following the Mw7.1 mainshock. The stars show the location of the 2019-*

366 *07-04 (Mw6.4) and the 2019-07-04 (Mw 7.1) earthquakes. The red rectangle in the inset figure*

367 *represents the studied area. LLFZ= Little Lake Fault Zone. CR= Coso Range. CA=California*

368 *State. NV= Nevada State.*

TEMPORAL VARIATION OF B VALUE, FORESHOCK ANALYSIS AND THE ROLE

OF FLUID

371   As mentioned before, the high quality of seismic catalogs of the Central Apennine and

372 Southern California regions allows us a robust estimation of the variation of cracks intensity

373 before, during, and after a moderate to strong earthquake and therefore permits a detailed

374 analysis of foreshocks activity prior mainshocks. The relation between the temporal variation

375 of the b-value, foreshocks occurrence, and fluid migration shows that the decrease in b-value

376 may correlated with the dilatancy-fluid diffusion process that precedes a large earthquake

377 (Scholz & Kranz, 1974; Scholz, 2019). Based on a laboratory scale acoustic emissions analysis

378 and fracture mechanics modeling of rocks failure under water-saturated conditions, the increase

379 in stress concentration during the final stage of dilatancy and the beginning of fluid diffusion

380 on a dominant rupture occurs when the b-value is lower than 1 (Main *et al.* 1990). The decrease

381 in the b-value is also connected to the strain softening and shear localization during the

382 occurrence of the foreshocks sequence (Main et al. 1990).

383   In order to explore in detail, the role of fluid before and after a large earthquake, I compare

384 simultaneously the temporal evolution of the b-value in the Central Apennine with those

385 following the 2019 Ridgecrest sequence. The analysis of the temporal evolution of the b-value

386 includes four major sequences: the 1997 Colfiorito (Umbria Marche) sequence, the 2009

387 L'Aquila sequence, and the 2016 Amatrice-Norcia sequence, and the 2019 Ridgecrest

388 sequence. To better constrain the b-value time series and as mentioned before, I use the high-

389 resolution catalog proposed by the Istituto Nazionale Di Geofisica E Vulcanologia (INGV)

390   combined with the Gasperini et al. (2013) and the Tan et al. (2021) catalogs for the Central

391   Apennines and the highest confidence QTM seismicity catalog for Southern California (Ross

392   et al. 2019) aided by the Shelly (2020) catalog for events that occurred during the 2019

393   Ridgecrest sequence as a seismic input to the b-value time series modeling. The b-value time

394   series technics consists of analyzing the frequency-magnitude distribution of earthquakes over

395   variable time windows. This approach based on a fixed number of events allows for better

396   estimates of the variation of the b-value at each point in time which leads to better constraining

397   the evolution of seismicity in a region with a high variation in seismicity rate through different

398   time scales (Tormann et al., 2013). If we suppose that the b-value time series is defined as a

399   temporal representation of crack distribution in a seismogenic zone, then the b-value magnitude

400   for each time windows interval is selected with respect to the distribution of the magnitude of

401   completeness (Mc). The Mc value is assessed for each window interval (with specific N=250

402   events) after a recutting level, established using the maximum curvature method with a

403   correction factor of 0.2 for safety. The b-value times series is computed for selected windows

404   using the maximum-likelihood estimates (Wyss & Wiemer, 2000). I also consider the temporal

405   change in Mc in the b-value time series computations following each main event in order to

406   minimize the dependence of the b-value times series from Mc in the selected time windows.

407   To better constrain the evolution of seismicity near Ridgecrest, I combine the QTM catalog

408   during the entire period of 2008-2017 with the USGS seismicity catalog covering the period

409   from January 2017 to Mai 2020. The seismicity database also includes the 2019 Ridgecrest

410   precise relocation catalog of Shelly (2020). Similar events due to the combination of different

411   catalogs are detected and eliminated automatically using the Zmap software (Wiemer, 2001).

412   The Ridgecrest zone is divided into 0.15° x 0.15° grids and the events were selected using a

413   variable time windows approach. The computation is made regarding the approach based on a

414   fixed number of events of 250 with a 50 minimum event higher than the local value of Mc by

415   using the Maximum curvature method with magnitude binning equal to 0.1. Considering the

416   change in the Mc value and for the Ridgecrest earthquake sequence, I obtain an Mc value range

417   of [0.84, 1.4] before the Mw 6.4 event and [0.66, 1.2] from the period between the Mw 6.4 and

418   Mw7.1 mainshocks. After the Mw7.1 event, the Mc value range between [0.4, 1.2]. In order to

419   reduce uncertainties on the b-values estimations, and as mentioned before, I asses Mc using the

420   maximum curvature approach and I add 0.2 to the value of Mc. I confirm that the value of Mc

421   that gives a reasonable estimate of the temporal evolution of the b-value is about 1.4, in the

422   same order as the value proposed by Gulia et al. (2020) for the same sequence. I also verify that

423   the temporal b-value estimates do not change considering an Mc range of [1.1,2.0]. The same

424   approach is made for the sequences that occurred in Central Apennines.

425   The temporal evolution of the Mc-value with the distribution of the b-value is evaluated

426   simultaneously at appropriate time windows in order to reduce uncertainty in the b-value

427   estimates. The b-value time series are performed for a number of events $50 \leq N \leq 500$ enables us

428   an appreciable degree of smoothing/damping signals (Figs. S8 & S9). The temporal evolution

429   of the b-value is based on the earthquake occurrence time approach using a window size range

430   between 50 to 500 events, which yields an interval sampling rate of approximately 1-12 months.

431   The b-value time series shows that the shape of the time series is preserved for $100 \leq N \leq 500$

432   for both the 2016 Amatrice-Norcia and 2019 Ridgecrest sequences (Figs. S8 & S9). These

433   results are relatively the same as those obtained by Wyss & McNutt, (1998) in analyzing the

434   1989 earthquake swarm beneath Mammoth Mountain (CA) or by Tormann et al (2013) in the

435   modeling of the temporal correlation between the change in the b-value and surface creep of M

436   6 series of events occurred in Parkfield (CA).

437   Figure 4 shows the preferred b-value time series for the Ridgecrest case. The optimum time

438   series calculation is made with a sample size of 250 events at a low window overlap (~4%).

439   Considering the Mw6.4 earthquake sequence as a Foreshock sequence, the temporal evolution

440   of the earthquake size distribution shows an increase in b-value one year before the 2019

441   Ridgecrest sequence followed by a gradual decrease in b-value ~ one month before the Mw 6.4

442   foreshock (Figures 4 and 5). After the Mw 6.4 earthquake, the b-value rapidly varies from

443   minimum to maximum and from maximum to minimum just before the Mw7.1 earthquake

444   showing major double picks (Figures 4C and 5A) as predicted by the laboratory experiments in

445   water-saturated specimens (Main et al. 1989). The sudden increase in b-value before the Mw

446   7.1 earthquake as observed in Figures 4 and 6A is interpreted as a response to pore pressure

447   drop during the undrained phase of the fluid. This value is close to the value of b ~ 1 during the

448   left lateral earthquake but the increase in aftershock productivity caused by fluid migration and

449   pore pressure instability in the ~ 33 hours preceding the Mw7.1 right lateral earthquake tends

450   to re-decrease the b-value to ~ 0.5 creating a double b-value minima as observed in Figures 4C,

451   5A, 5C and 6A.

452   The presence of off-fault damage accumulation and fluid redistribution tends to decrease

453   rapidly the b-value and creates a slip instability promoting the next Mw7.1 failure (Figures 4,

454   5, and 6A). In this case, the minimum doublet b-value as observed in the b-value time series

455   may be interpreted as a local dilatancy hardening phase resulting from fluid migration along

456   conjugated fault ruptures. At this time, the fluid migration at a short time-scale requires a

457   significant evolution of the permeability along fault ruptures. Based on this assumption and

458   other considerations in relation to the stress change induced by fault geometries in a spring-

459   slider model for dilating fluid-infiltrated fault (Segall & Rice, 1995; Chambon & Rudnicki,

460   2001), the temporal fluctuation of the b-value related to the 2019 Ridgecrest sequence seems to

461   be controlled by slip instability due essentially to the pore pressure fluctuation caused by fluid

462   migration along the heterogeneous fault zone.

463
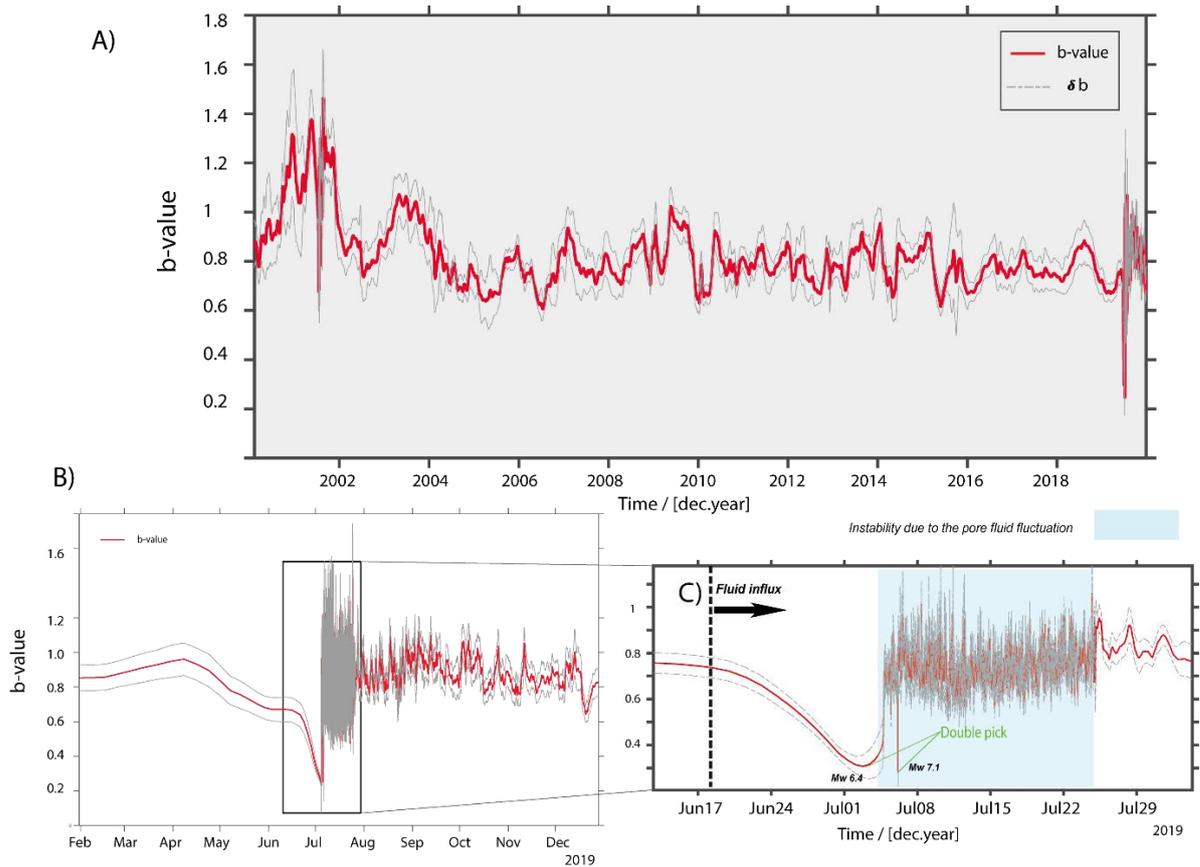
Figure 4*: Earthquake size distribution estimates for the Ridgecrest fault zone area. **A)** b-value time series spanning the period from 2000 to 2020 using the highest confidence QTM seismicity catalog for Southern California (Ross et al. 2019) combined with the high definition USGS-NEIC catalog. The identical events were found and automatically fixed using the Zmap software. The b-value time series were computed using the maximum curvature approach for a moving window of 500 events with a step size of 50 events. The window overlap is fixed at 4%. The Standard deviation of the b-value (δb) is represented by a dashed grey line and is obtained using the maximum likelihood estimation approach (Shi & Bolt 1982). **B)** Zoom-in figure for the period from February 2019 to January 2020. **C)** Zoom-in figure for the period from ~ 2 weeks before the 2019 Mw 6.4 first earthquake to August 01, 2020, but by adding a high smoothing plot factor (~ 6) to the b-value estimations.*

474

Note that the temporal b-value instability associated with the pore pressure fluctuation continues during the two months following the Mw7.1 earthquake (Figures 4B and C). The ~

477 two-month instability period may also represent the duration of the Mw 7.1 poroelastic rebound.

478 Also, the similarities between the temporal evolution of the b-value for the 2019 Ridgecrest and

479 the 2016 Amatrice-Norcia sequences (Figure 6 A and B) may suggest an analog physical

480 mechanism controlling the foreshock occurrence for both sequences.
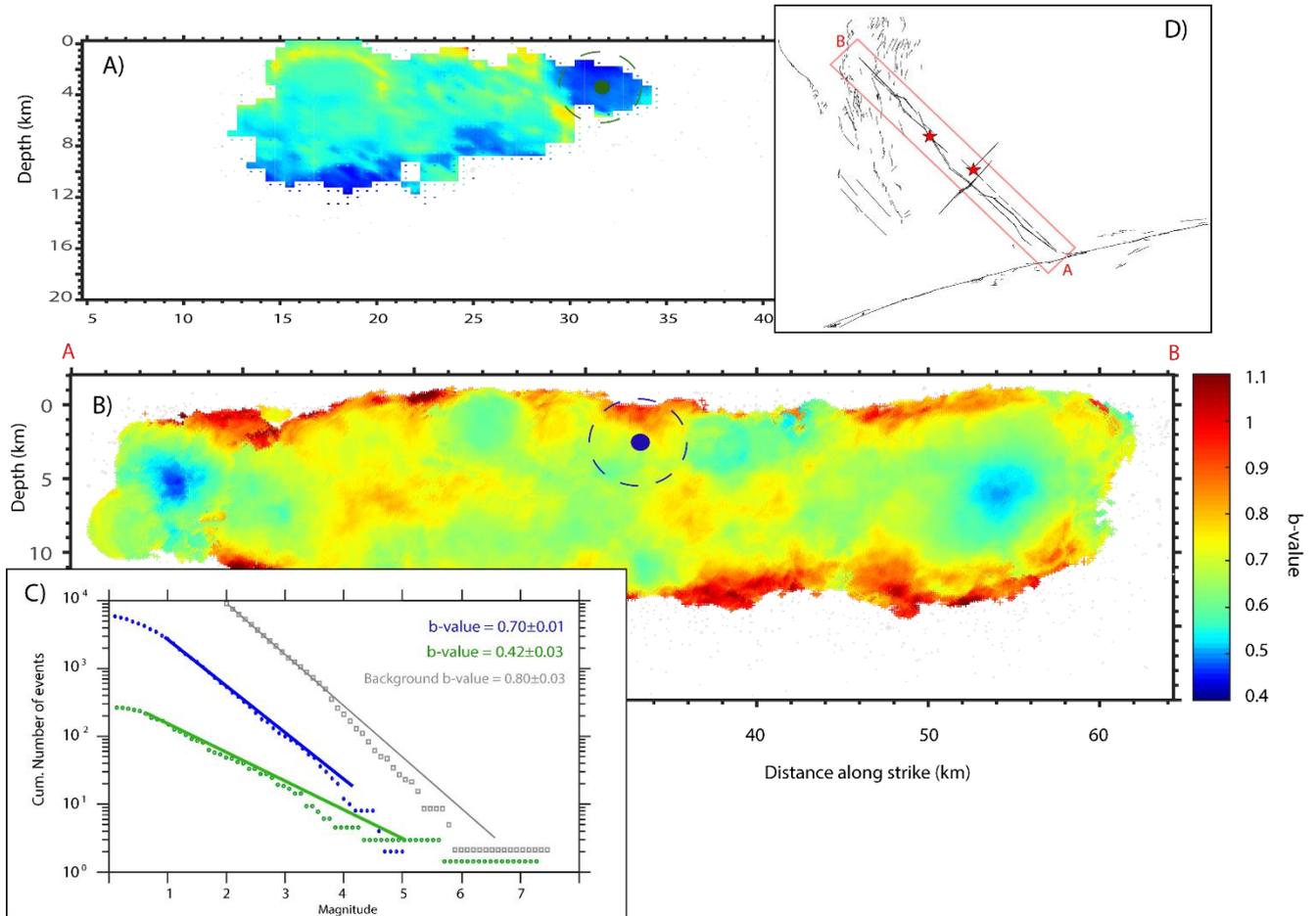
481

482 **Figure 5***: Spatio-temporal evolution of the b-value associated with the 2019 Ridgecrest sequence: **A)**

483 *cross-section showing b-value distribution before the Mw7.1 earthquake. **B)** Cross-section showing a*

484 *b-value distribution after the Mw7.1 earthquake. **C)** Frequency-Magnitude Distributions (FMD)*

485 *around the Mw7.1hypocentral area before and after the Mw7.1 event: the green curve represents the*

486 *G-R distribution before the Mw7.1 event, the blue curve represents the G-R distribution after the*

487 *Mw7.1 and the gray curve represents the background FMD distribution. The dashed colored circles in*

488 *A) and B) represent the locations of events used in C). **D)** Position of the cross-section with respect to*

489   *the surface distribution of the Ridgecrest fault ruptures. The Ridgecrest Fault-ruptures are from Xu et*

490   *al., (2020). The Quaternary faults are from the USGS.*

491   Indeed, the b-value anomalies as in figure 6B also coincide with the hydrogeological and

492   geological anomalies observed in the months before and during the onset of the Amatrice-

493   Norcia sequence (Barberio et al.,2017). These anomalies are interpreted as the consequence of

494   a deep crustal fluid migration along major active ruptures (Barberio *et al.* 2017). The

495   hydrogeochemical changes observed in a group of springs in the central Apennines (Barberio

496   *et al.* 2017) with the increase in the content of Cr, Fe, and V in a calcium carbonate aquifer

497   during the months before the 2016 Amatrice-Norcia sequence also agree with the change in

498   earthquake size distribution (Figure 6B) and denote clear evidence of fluid migration

499   following the 2016 Amatrice-Norcia sequence. Also, the double b-value minima as observed

500   in figure 6B correlates with the relative crustal velocity fluctuation observed in Amatrice-

501   Norcia seismogenic zone (Soldati et al., 2019).

502   Considering the case of the 1997 Colfiorito sequence, the gradual decrease in b-value prior

503   to the foreshock sequence (Figure 7C) seems to be concordant with the fracture model of Main

504   et al. (1990). Adopting the Main et al (1990) experimental model of cracks, the temporal

505   evolution of the b-value may be defined here as a rapid failure after periods of strain hardening

506   and strain softening due essentially to the pore-fluid diffusion process. The dilatancy softening

507   phase related to the 1997 Colfiorito sequence seems to be controlled by the fluid migration

508   along fault zones where the stress intensity is highly coupled to the temporal variation in

509   effective normal stress. Considering the Terzaghi Law, the fluid diffusion phase will play a

510   crucial role in accelerating seismicity by decreasing the magnitude of effective normal stress

511   acting along cracks promoting the occurrence of fast slip episodes at a short time scale.

512 The time evolution of the b-value following the 2009 L'Aquila sequence differs from those

513 obtained for the 2016 –Amatrice-Norcia and the 2019 Ridgecrest sequences (Figure 6 and 8).

514 This difference may be due to the presence of a large deep fluid reservoir near L'Aquila fault

515 zone which maintains a high pore fluid pressure during a large period of time. Indeed, the

516 InSAR time series analysis related to the central Appenine earthquakes reveals that the

517 sedimentary basin nearby the L'Aquila fault zone had experienced about 10 mm of accelerating

518 subsidence in the years prior the L'Aquila mainshock (Moro *et al.* 2017) in agreement with the

519 observed change in the frequency of the b-value time series (Figure 8).

520 The accelerating subsidence is viewed as a consequence of large pre-earthquake fluid

521 migration along the fault zone (Moro et al. 2017). Based on our estimation of the b-value

522 (Figures 7 and 8) and ground deformation estimated from SAR imagery (Moro et al. 2017), the

523 acceleration of subsidence is interpreted here as probably due to large dilatancy-fluid diffusion

524 processes that control the temporal fluctuations of the b-value at a large time scale. The analysis

525 of the Time-magnitude series shows a gradual decrease in the number of events with magnitude

526 M<3 associated with an increase of events with magnitude >3.5 in good agreement with the

527 change in the b-value time series (Figures 7 A and 8). A second phase with an apparent increase

528 of small magnitude earthquakes accompanied by a decrease in the number of events with a

529 magnitude Mw larger than 3.5 is observed in the ~ months prior to the 2009 L'Aquila

530 mainshock (Figures 7 A and 8). The gradual increase of micro-seismic events observed in the

531 two months prior to the L'Aquila mainshock is highly coupled with the gradual decrease in the

532 b-value (Figure 8).
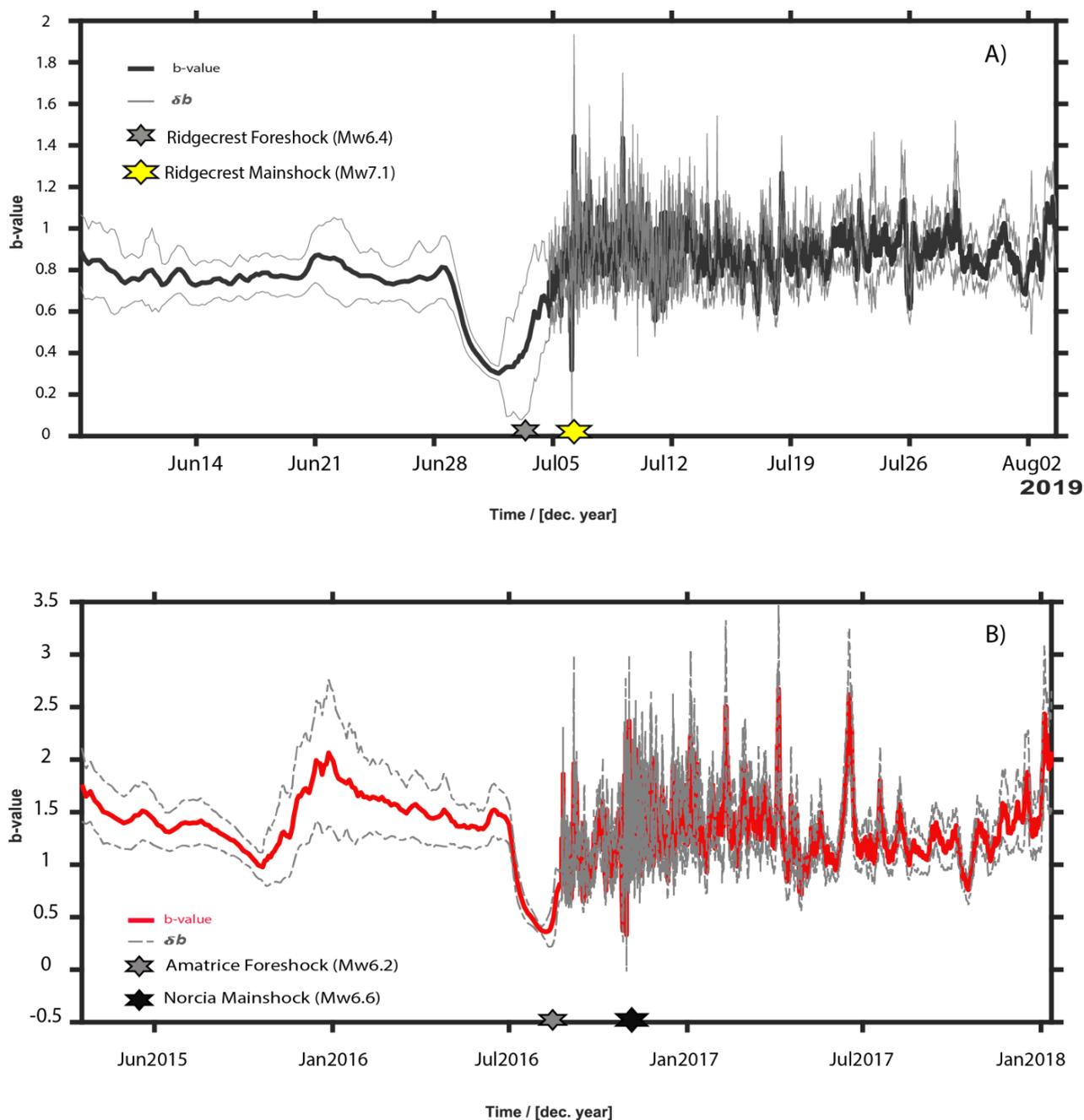
Figure 6*: Comparison between b-value time series analysis following: **A)** 2019 Ridgecrest sequence and **B)** 2016 Amatrice-Norcia sequence. The two figures show a double pick during the foreshock – mainshock period as predicted by the laboratory experiments on water saturated specimens. The b-value time series is performed using the combined high resolution NEIC-USGS catalogs and supplemented by the Shelly (2020) catalog for events that occurred during the 2019 Ridgecrest foreshock-mainshock sequence. The b-value time series for the 2016 Amatrice-Norcia sequence is performed using the entire catalog of the INGV combined with the local catalogs published by Gulia et*

541   *al. (2019). The b-values time series are computed using ZMAP7.0. For both sequences, the uncertainty*

542   *estimation is obtained by 100 bootstraps related to windows size of 200 events. The windows overlap is*

543   *fixed at 2 %.*

544
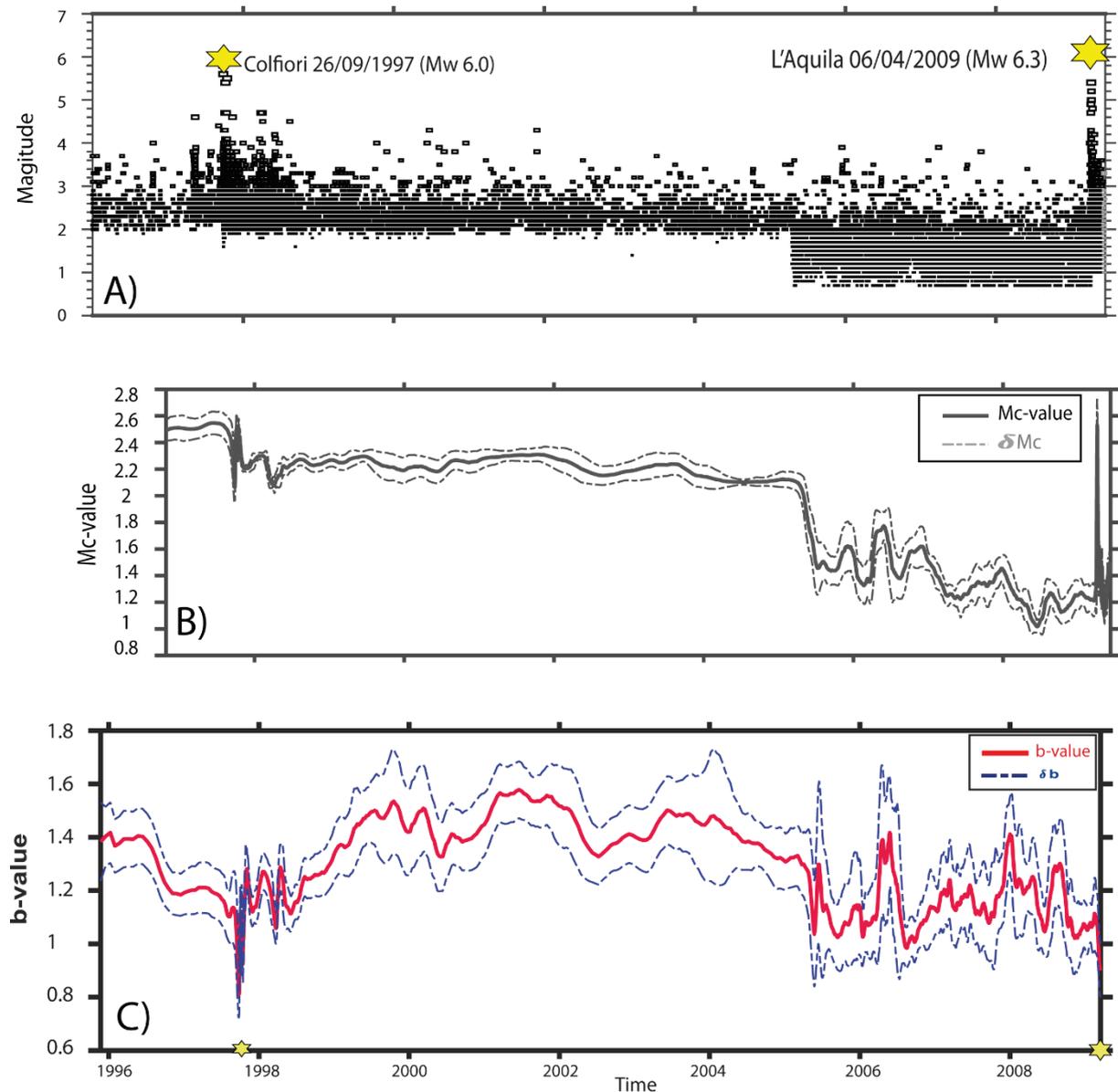
545

546   **Figure 7.** *A)   Earthquake magnitude versus time for the central Appennines covering the periods*

547   *between 1996 to 2009 and using combined catalogs of INGV and Gasperini et al (2013) catalogs. The*

548   *yellow stars represent the position of the 2019 Mw 6.0 Colfiorito and the Mw6.3 L'Aquila mainshocks.*

549   *B) Mc-value time series using the same catalogs as A) and covering the periods between 1998 to 2009.*

550   *The magnitude of completeness (Mc) varies in times from 2.5 (before 1997) to 1.4 (after 2005) with*

551   *uncertainties δMc equals to 0.15 and 0.18 respectively. **C**) Temporal evolution of the G-R b-value in the*

552   *central Appennines covering the same periods as in A. The shape of the b-value time series as proposed*

553   *here and taking into account the temporal variation of Mc is similar to the b-value computation by*

554   *supposing a fixed Mc value of 2.6 using N ~250 fixed sample size windows with 100 bootstraps.*

555   The tendency of the b-value time series during the last phase of the L'Aquila interseismic

556   period is interpreted here as an influx of pore fluid into a dilatant volume near the nucleation

557   zone. The increase in the magnitude of foreshocks just before the L'Aquila mainshock (Figure

558   8) affect considerably the temporal evolution of the b-value by creating a sudden drop in the b-

559   value. The Time-shift between the start of foreshocks and the b-value decrease seems to

560   correlate with the gradual increase in microseismic events followed by a sudden increase in

561   earthquakes with magnitude M>=3.0 (Figure 8). This complex distribution of events may be

562   seen as a complex evolution of the effective stress drop denoting a complex earthquake

563   preparation conjugated to a complex distribution of the fluid flow process in a heterogeneous

564   fault zone.

565

566
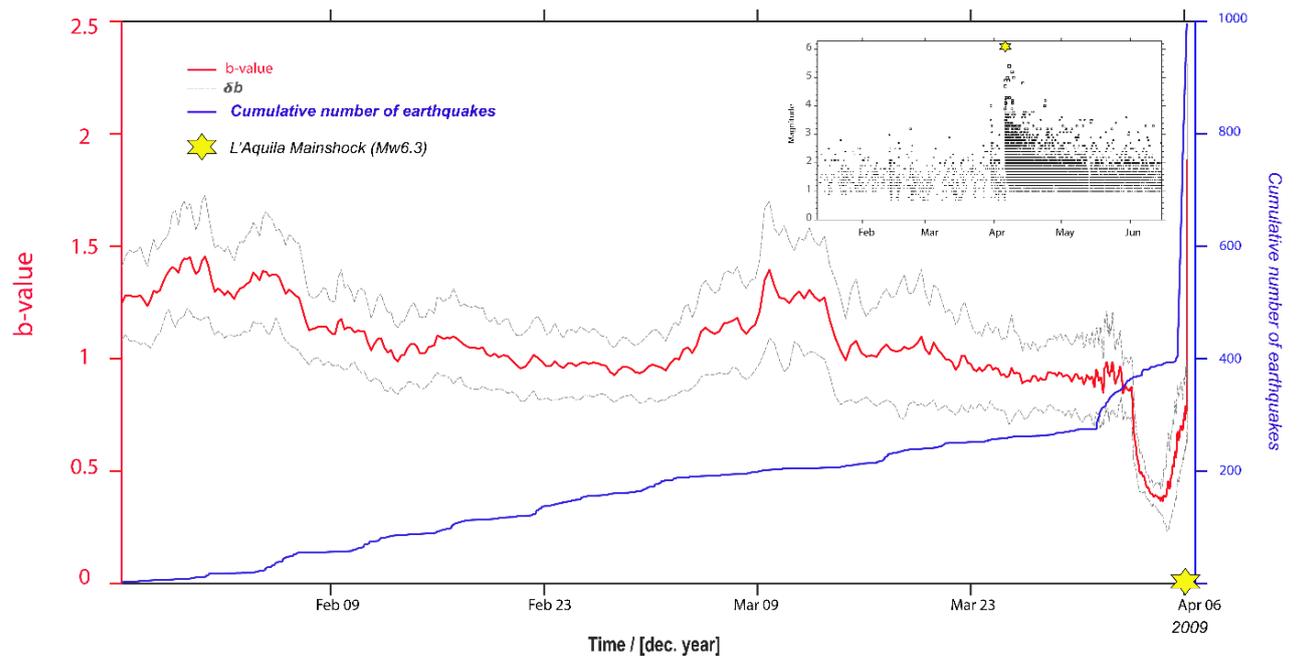
Figure 8 *Temporal evolution of the G-R b-value (in red) and the cumulative number of earthquakes (in blue) during the Foreshock period priors to the Mw6.3 L'Aquila earthquake using the entire catalogs of Gasperini et al (2013). The b-value time series is obtained using a sample windows size of 150 events with 100 bootstraps. For safety, the Mc correction value is fixed at 0.2 comparable to the value used for the predictive foreshock model of Gulia et al (2016). The black stars represent the position of the Mw 6.3 L'Aquila mainshock.*

STRESS ANALYSIS, TEMPORAL EVOLUTION OF AFTERSHOCK AND THE WEAKNESS OF ACTIVE FAULTS

As shown in the previous section, the occurrence of moderate to strong earthquakes along the SWL-ECSZ and Central Apennines zones may be coupled with the fluid migration along heterogeneous fault zones causing abnormally elevated pore pressure and promoting the occurrence of moderate to large earthquakes. Based on the Coulomb failure criterion, the dynamic poroelastic stress change modeling following the Ridgecrest Mw6.4 left lateral event shows a high value of stress at the nucleation area of the Mw 7.1 right-lateral rupture (Figure

582   9A) when the purely elastic stress modeling predicts an absence of earthquake activities (Figure

583   9B**;** Lozos & Harris, 2020; Kariche, 2022). One of the possible explanations for the temporal

584   evolution of stress change values from negative to positive as shown in figure 9 is the fluid

585   redistribution along conjugated fault ruptures which creates favorable conditions for a

586   weakening mechanism by increasing pore-fluid pressure along the right-lateral major fault

587   rupture and in fact, promoting the occurrence of the Mw7.1 earthquake. The rupturing process

588   on conjugated strike-slip faults assisted by fluid migration is not unusual. Using a typical

589   undrained and drained Poisson ratios for a Berea sandstone, the modeling of the Coulomb

590   failure function per unit of stress drop caused by the 1987 Elmore-Ranche event (Mw 6.2) on

591   the conjugated Superstition Hills fault (Mw6.6) show a maximum stress value in the ~11 hr

592   following the Mw 6.2 event (Hudnut et al, 1989). For the 2019 Ridgecrest sequence, the

593   Coulomb stress change modeling taking into account the effect of fluids reveals that the ~33hr

594   time delay between mainshocks may viewed as a triggering mechanism controlled by the fluid-

595   flow process (Figure 9A; see also figure S5 on Kariche, 2022). The value of fluid diffusivity is

596   relatively low to the value obtained for the Superstition Hills sequence (Kariche, 2022) and may

597   denote that the fluid migration along faults controls the time delay between earthquakes.

598
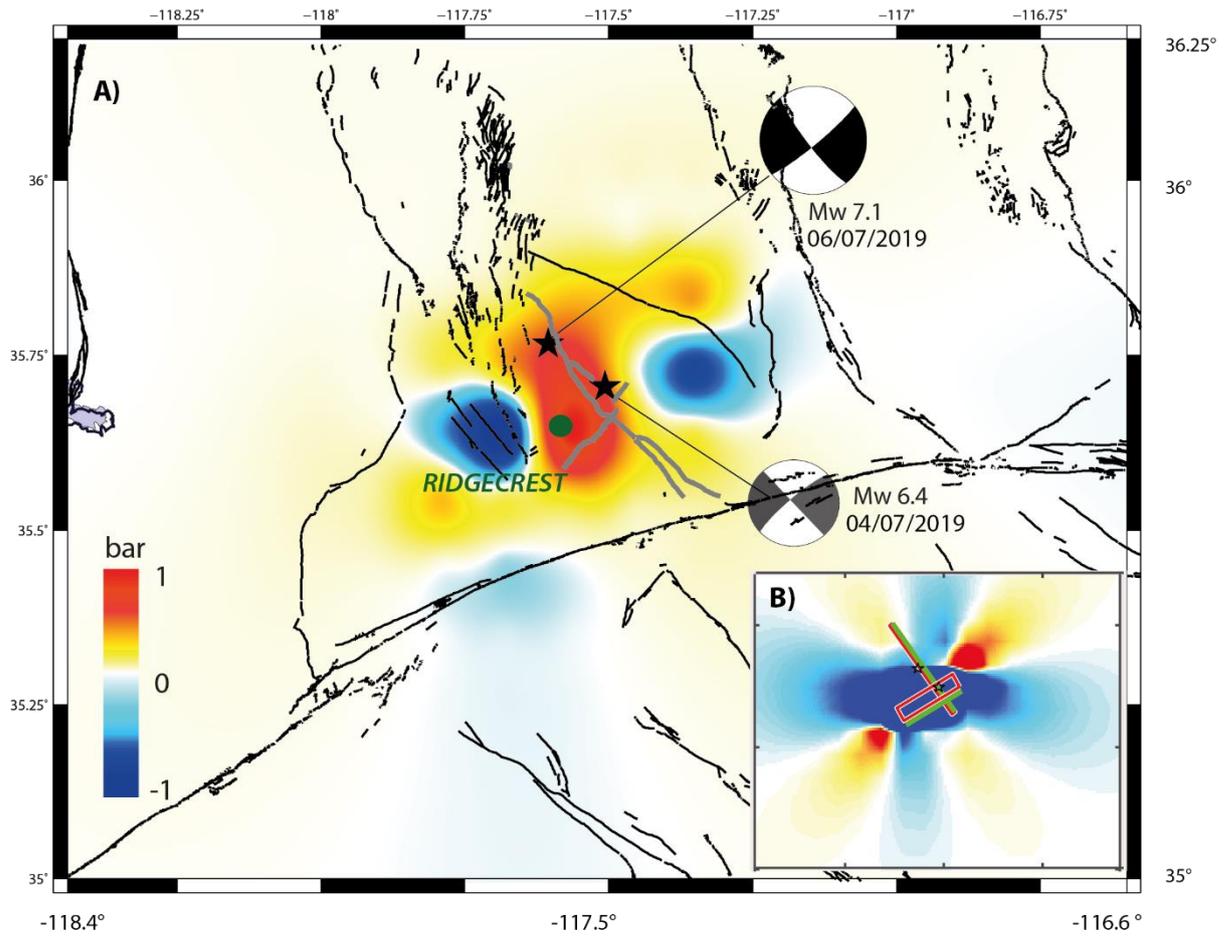
Figure 9: *A) Short–term poroelastic stress change modeling following the Mw6.4 earthquake on receiver fault planes with Strike /Dip/ Rake = 143°/85°/-165° at 8km depth. The post-seismic stress redistribution following the 04-07 (M6.4) from the undrained state to the drained fluid state using extreme undrained and drained Poisson ration values (vu, v = 0.31, 0.15). These values are interpreted as a consequence of a high variation in rock rheology before and during the Mw6.4 earthquake. B) Co seismic stress transfer caused by the Mw6.4 earthquake on receiver fault planes with Strike /Dip/ Rake = 143°/85°/-165 at 8 km depth. The co-seismic stress modeling is performed using simple conjugate fault geometries.*

Considering a model of friction which assumes that the frictional stress σ_f is proportional to the shear stress magnitude after an earthquake, and if we argue that the stress difference following an earthquake is coupled to the radiated wave energy E_s, then an average dynamic stress drop $\Delta\overline{\sigma_d}$ can be expressed by using the simple solution as (Kanamori ,1994):

611
$$\Delta\overline{\sigma_d} = \frac{E_s\ (J)}{M_0\ (N.m)} \times 2\mu\ \ldots\ldots(9)$$

612   where μ is the rigidity and M_0 is the seismic moment.

613   The radiated energy can be estimated by using the equation (Kanamori, 1994):

614
$$E_s\ (J) = \frac{1}{2}\ S\overline{D}\ (\sigma_0 - \sigma_1).\ \ldots\ldots..(10)$$

615   where S represents the surface area of the crack, $\overline{D}$ represents the average crack displacement

616   during an earthquake and the $\sigma_0 - \sigma_1$ is defined as the differential stress. The value of $E_s\ (J)$

617   can also be obtained directly by analyzing the seismic wave form.

618   By using equation 9 and 10 for a value of M_0 and Es deduced from the 2019 Ridgecrest

619   source time functions extracted from the Incorporated Research Institutions for Seismology

620   (IRIS), I estimate an average dynamic value of stress drop for the Mw 7.1 Ridgecrest earthquake

621   as equal to $\Delta\sigma_d$ ~ 20 bars for a coefficient of rigidity ~ 3.10^{11} dyne/cm^2. This value is ~ three

622   times less than the value of static stress drop $\Delta\sigma s$ for the same event obtained by joint focal

623   mechanism, GPS , and InSAR data (Barnhart *et al.* 2019; Sheng & Meng 2020). The value of

624    $\Delta\sigma_d$ for the Ridgecrest main event is relatively low compared to those obtained by Shearer *et*

625   *al.* (2006) for the major earthquakes that occurred in Southern California. Even so, the temporal

626   anisotropy in stress drop following Ridgecrest (from static to dynamic) concurs with spatial

627   heterogeneity in the stress drop along the SWL-ECSZ (Shearer *et al.*,2006; Hauksson, 2015).

628   The analysis of a large set of focal mechanisms in the SWL-ECSZ shows a high anisotropy in

629   stress drop distribution from the Garlock fault zone to Ridgecrest (Hauksson, 2015). The stress

630   drop starts low near the left lateral Garlock fault, increases to the northwest near Ridgecrest

631   faults, and finally, reaches the minimum at the Coso geothermal area (Hauksson, 2015). Also,

632   the spatial variation in stress drop is in good agreement with the rotation of the maximum

633   horizontal stress (SHmax) (Yang & Hauksson, 2013). The variation in stress drop combined

634   with the SHmax rotation may suggest the presence of weak zones outside the Ridgecrest

635   conjugate fault systems which are probably connected to an abnormal fluid pressure due to fluid

636   migration at depth. According to the time-dependent composite model of Kanamori (1994), the

637   decrease in stress drop from static to dynamic following the Mw7.1 Ridgecrest earthquake may

638   be interpreted as a result of a dynamic weakening mechanism caused essentially by abnormal

639   fluid pressure. In this case, the stress drop starts in the same order as the static stress drop and

640   decreases in time during the pore-fluid pressure redistribution.

641   The elevated pore pressure due to the fluid migration in heterogeneous fault zone tends to

642   affect the value of permeability and creates an area with a low-stress drop tendency. Based on

643   the poromechanical model of Byerlee (1992), I found that the permeability along the Ridgecrest

644   fault zone increases by a factor of 10^3 following the Mw7.1 mainshock. Similar results

645   including causative relations between the evolution of pore-fluid pressure and the variation in

646   stress drop are also found in analyzing stress anomalies on major active faults in Southern

647   California (Bird, 2017) and in fault strength analysis of active fault ruptures (Copley, 2018).

648   Based on these considerations, the temporal and spatial evolution in stress drop can not only be

649   explained by the variation of the frictional property of rocks. Our results tend to validate the

650   role of fluid in controlling both nucleation and the size of major fault ruptures in the SWL-

651   ECSZ (Tong et al., 2021; Kariche, 2022). Note that the possible role of pore pressure variation

652   on the complex distribution of stress drop during the 2019 Ridgecrest sequence was also

653   examined by Trugman, (2020).

654   The fluid migration during an earthquake may also affect the productivity of aftershocks.

655   Figure 10 shows a comparison between the cumulative stress change modeling caused by the

656   full poroelastic relaxation of the Mw7.1 Ridgecrest using different values of drained υ and

657   undrained υu Poisson ratio and the spatial distribution of aftershocks following the Mw7.1

658   Ridgecrest earthquake. Figure 10 (A, B, and C) shows a correlation between: 1) the evolution

659   of stress change following the Mw 7.1 earthquake, 2) the fluid diffusion process and 3) the

660   spatial distribution of a part of aftershocks nearby and at NNW of the Mw7.1 epicenter. The

661   values of υu and υ used in Figure 10 might be associated with water-saturated rocks in the upper

662   few kilometers of the seismogenic zone (h≤ 15km). The fluid-diffusion process associate to the

663   2019 Ridgecrest sequence is supposed to act locally (Figures 9 and 10). The Coulomb stress

664   change modeling result at half of the seismogenic zone and taking into account the diffuse effect

665   of fluids shows an increase in stress change values near the epicentral area of the Mw7.1 event

666   (Figure 9A). Also, the full poroelastic relaxation caused by the Mw7.1 of faults parallel to the

667   main rupture seems to mimic the spatial distribution of aftershocks at the northern part of the

668   Mw7.1 main rupture (Figure 10A, B, and D). On the contrary, for the southern part of the

669   Mw7.1 Ridgecrest fault zone, the triggering mechanism seems to be independent of the fluid

670   diffusion process (Figures 10 A, B, and C). These results agree with the idea that the aftershocks

671   generation following the 2019 Ridgecrest earthquake is complex and may relate to both afterslip

672   and poroelastic relaxation processes. Indeed, the analysis of the co and the early postseismic

673   surface deformation (~ 2 months of deformation) following the 2019 Ridgecrest shows that the

674   ~ one month observed postseismic deformation is associated with both afterslip and poroelastic

675   rebound (Wang & Bürgmann, 2020). Based on the surface deformation analysis (Wang &

676   Bürgmann, 2020) and stress change modeling results (Figure 10), I suggest that the seismicity

677   rate associated with the southern part of the Mw7.1 main fault is mainly defined as a model

678   based on afterslip evolution as reported by the time series analysis from the B921 strainmeter

679   located in the same area (Hirakawa & Barbour, 2020) while the early aftershock generation in

680   the northern part seems to be mainly due to the poroelastic rebound of the Mw7.1 mainshock

681   (Figure 10 B and D).

682
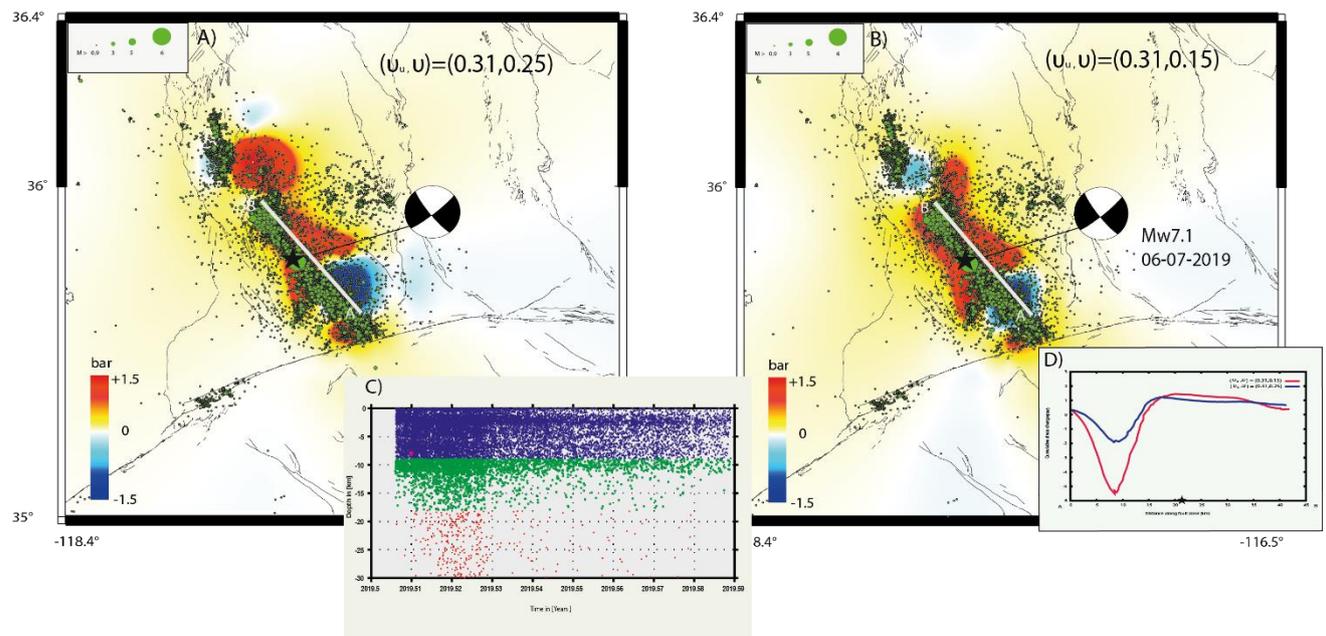
Figure 10: *Cumulative stress change due to the full poroelastic rebound following the Mw7.1*

Ridgecrest earthquake on right lateral fixed receiver fault planes parallel to the Mw7.1 main rupture.

A) poroelastic stress change modeling using a typical value of undrained and drained Poisson

ratio(υu,υ)=(0.31,0.25). B) poroelastic stress change modeling using the extreme value of undrained

and drained Poisson ratio (υu,υ)=(0.31,0.15). C) Temporal evolution of seismicity at depth following

the 06-07-2019 (Mw 7.1) mainshock. D) Poroelastic stress change profiles caused by the full relaxation

of the Mw7.1 earthquake along parallel right-lateral fault ruptures. The seismicity databases are from

NEIC-USGS. The stress change modeling is fixed at 8 km depth.

691

In order to explore in detail, the mechanism of post-seismic deformation following the 2019

Ridgecrest sequence and related fluid migration, I analyze the temporal evolution of the

aftershock frequency rate associated with the Mw7.1 earthquake and I compare it with the

case of the central Apennines. Figure 11 shows a comparison between the effect of fluid

redistribution on aftershocks occurrence following the Mw6.0 Colfiorito and the Mw7.1

Ridgecrest earthquakes. Figure 11 (A and C) shows strong similarities between the temporal

evolution of the aftershock sequence following the two earthquakes (Figure 11 A and C). The

699   aftershock frequency rate curve starts with a rate decay of $1/\sqrt{t}$, while it became equal to $1/t$ in

700   days to one month after the 1997 Colfiorito and Mw7.1 Ridgecrest mainshocks as predicted

701   by the pore-fluid diffusion equation (see equation 8 in the methodology section). Based on the

702   pore fluid flow hypothesis, the $1/\sqrt{t}$ decay is interpreted as an increase in aftershocks

703   productivity due to the pore fluid diffusion along the fault zone. Figure 11C shows that at a

704   short-time scale, a part of the aftershocks productivity is controlled by the fluid migration

705   along the fault zone creating an aftershocks expansion area inside and outside the main

706   Ridgecrest fault plane. The increase in aftershocks productivity is also observed in Omori fit

707   curve when the seismicity rate shows additional aftershocks in the ~ 10-20 days after the

708   Mw6.0 Colfiorito and in the ~ 5-20 days after the Mw7.1 Ridgecrest mainshock (Figure 11B

709   and D) which cannot be explained by the aftershock rate decrease as predicted by the Omori

710   Law. These results are also validated by the abnormalities in aftershock activity observed in

711   monitoring the temporal and spatial seismic activity following the Mw 6.4 Ridgecrest

712   earthquake (Ogata & Omi, 2020). In addition, the duration of the increase in aftershocks

713   activity (Figure 11D) seems to follow the duration of pore-fluid instability as estimated by the

714   b-value time series (Figure 4C). Note that the underproduction of aftershocks as seen just after

715   the Mw7.1 mainshock (Figure 11C) may due to the under-reporting of small events in relation

716   to the incompleteness of the seismic catalogs soon after mainshock.

717   The spatiotemporal distribution of aftershocks following the 2019 Ridgecrest earthquake

718   is complex (Ross *et al.* 2019; Trugmaan 2020). The complex slip distribution and the

719   heterogeneity in fault zone tend to maintain elevated fluid pressure and in fact, increase

720   aftershock productivity. These results are also valid for the Central Apennines sequences.

721
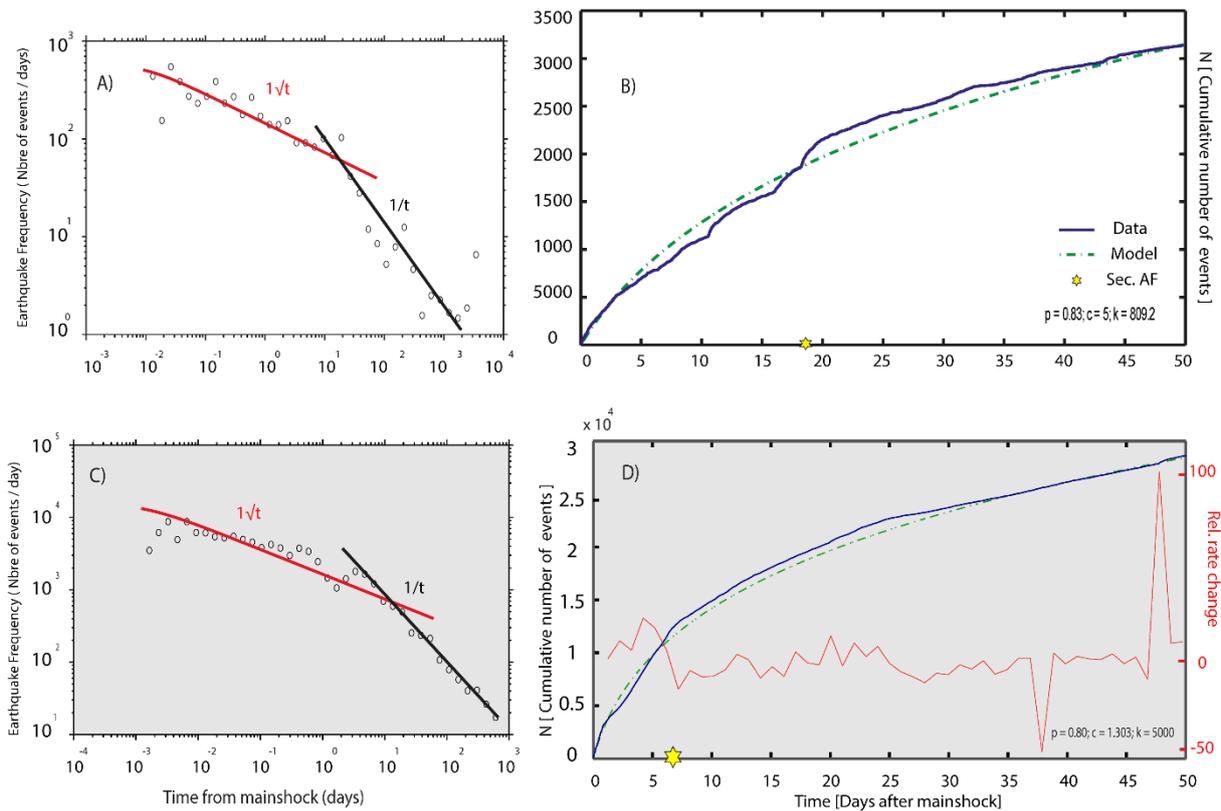
Figure 11: *Representation of the temporal postseismic effect following the Mw 6.0 Colfiorito and Ridgecrest earthquakes. **A)** Seismicity rate change versus time following the Mw 6.0 Colfiorito earthquake. **B)** Comparison of observed seismicity (blue) and the Omori fit (green) using the Zmap algorithm for 50 days' time windows following the Mw6.0 Colfiorito mainshock. **C)** Seismicity rate change versus time following the Mw 7.1 Ridgecrest earthquake. **D)** Comparison of observed seismicity (blue) and the Omori fit (green) following the Mw7.1 Ridgecrest mainshock using the Zmap algorithm for 50 days' time windows. For the aftershock frequency vs time curves, the value of c is fixed to 0.01 d for Panels A and C and suppose variable (from 2.4 to 5) for Panels B and D. The yellow stars represent the position of the second major choc for each sequence. The relative earthquake rate change (red curve in D) is obtained from the change in slope of the cumulative number curve using a Habermann function regardless of the time of greatest change and comparing the rate in the two parts of the period (before and after the division point) by fit-time windows function (Wyss & Habermann, 1988;*

735   *Wyss & Wiemer 2000), the time variation function defines the variation between the rate before*

736   *and after at local time-scale.*

737   **DISCUSSION AND CONCLUSIONS**

738   The high quality of the Southern California and central Apennines earthquake catalogs

739   offers us the possibility to study in details the evolution of seismicity and related fluid migration

740   at different time scale. The evolution of seismicity near Ridgecrest and central Apennines

741   reveals that the temporal variation in b-value is probably due to the stress-fluid redistribution

742   along active faults. The b-value time series modeling shows a gradual decrease in the b-value

743   for all sequences. Based on previous laboratory experiments on water-saturated specimens

744   (Main *et al.,* 1990; Sammonds *et al*., 1992; Proctor et al., 2020), the gradual decrease in the b-

745   value may be interpreted as a dilatancy softening mechanism caused by an increase in pore fluid

746   pressure before each seismic event. The remarkable similarities between the evolution of the b-

747   value following the 2019 Ridgecrest and the 2016 Amatrice-Norcia sequences represented by

748   two b-value minima are probably due to similarities in mechanisms controlling the temporal

749   evolution of foreshock-mainshock sequences. The duration of the first b-value peak scale with

750   the magnitude of the first foreshock while the duration of the second peak (33 hr for Ridgecrest

751   and 4 days for Amatrice-Norcia) appears to be independent of the magnitude of related

752   foreshocks-mainshocks. Based on the coupled b-value –stress intensity laboratory experiments,

753   the duration of the second picks may be interpreted as a short term poroelastic stress

754   redistribution following a fast slip episode. Also, the temporal evolution of b-value for the

755   Ridgecrest and the central Apennines fault zone seems to be in good agreement with the fracture

756   mechanics model of water-saturated specimens as proposed by Main *et al.* (1989) who predict

757   an increase in acoustic emission rate in the dilatancy fluid diffusion phase when the static and

758   dynamic stress drop are not necessarily equals. My estimation of the average dynamic stress

759   drop following the 2016 Ridgecrest earthquake is three times less than the static stress drop

760   obtained by Barnhart *et al.* (2019) from joint focal mechanism and GPS and InSAR data. Based

761   on a direct measurement of pore pressure by using a miniature pressure transducer placed on

762   hydraulically faults network, Proctor *et al.* (2020) show that the effect of pore fluid pressure

763   variation exerts a fundamental control on earthquake rupture initiation and may exceed the

764   change from static to dynamic frictional properties of ruptures as predicted by the rate and state

765   friction laws.

766   The idea that the fluids affect the change in the b-value is not inevitably contradicting the

767   explanation proposed by different authors that the b-value may act as a stress meter (e.g Goebel

768   et al., 2013; Scholz, 2015). The conceptual models proposed here suppose that the decrease in

769   the b-value before foreshock is followed by an acceleration in crack growth and eventually an

770   increase in differential stress over time. The only difference may relate to the modeling of the

771   stress evolution from the period between foreshock and mainshock where the acceleration of

772   crack front would expect a decrease in elastic stress. At this time, the decrease in elastic stress

773   is compensated by the increase in pore fluid pressure in time and therefore increases the

774   Coulomb stress change on the receiver faults responsible for large rupturing process. In this

775   study, the elevated pore-fluid pressure due to the fluid migration in heterogeneous fault zone

776   tends to affect the value of permeability and creates an area with a low stress drop tendency.

777   Also, the occurrence of the Mw7.1 Ridgecrest right-lateral earthquake is not necessarily

778   associated with the presence of a large deep fluid reservoir. The rapid fluctuation of the b-value

779   just before the Mw7.1 may denote a rapid influx of fluid from surrounding rocks creating a pore

780   fluid instability on nearby heterogeneous fault ruptures. The temporal evolution of fault

781   permeability and related pore-fluid diffusion appears to be a crucial element in the apprehension

782   of the difference in the time delay between earthquakes in the central Apennines and the SWL-

783   ECSZ. The variation in earthquake time delay from hours to days for our studied sequences is

784   in good agreement with the values of fluid diffusivity obtained following: the 1997 Colfiorito,

785   the 2016 Amatrice-Norcia, and the 2019 Ridgecrest sequences.

786   In the same register, Gulia *et al.* (2020) developed a real-time earthquake monitoring

787   system based on a traffic–light classification that uses the temporal change in b-value to

788   constrain whether an ongoing earthquake sequence represents a decaying aftershocks phase or

789   precursors to an upcoming large event. Dascher-Cousineau *et al.* (2020) published a paper that

790   points out that the methodology proposed by Gulia *et al*. (2020) gives results in terms of

791   evaluating the risk of a large impending earthquake during the Mw6.4 Ridgecrest foreshock,

792   this method fails to predict the onset of the Mw7.1 sequence. Also, Dascher-Cousineau *et al*.

793   (2020) show that for the case of the 2019 Ridgecrest sequence, anomalous earthquake

794   productivity in adjacent regions may affect the background b-values and generate a false alarm.

795   In this study, the b-value time series interpretation taking into account the poroelastic properties

796   of the seismogenic zone shows difficulties to establish a good correlation between the duration

797   of the foreshock activities and the magnitude of the next largest expected earthquake. Despite

798   the fact that the inverse dependency of the b-value and the applied stress appears to be a

799   reasonable interpretation of the b-value drop prior to the Italian and Californian sequences

800   (Gulia & Wiemer, 2019; Gulia et al. 2020), the fluctuations of the b-value following the 2019

801   Ridgecrest and 2016 Amatrice foreshock sequences characterized by a double minimum seem

802   to unfollow the hypothesis that the drop in the b-value before mainshocks is only due to the

803   presence of high-stress levels on receiver main ruptures. This means that the magnitude of the

804   large expected earthquake is probably controlled by the variations in pore-fluid pressure rather

805   than the maximum differential stress.

806   Based on our results, detailed knowledge of geological structures, substratum permeability

807   and a robust evaluation of the pore fluid effect with a better constrain of seismicity and strain

808 rate before and during seismic sequences in addition to the statistical forecast methods appears

809 to be fundamental for the seismic hazard assessment and any decision making.

810 **DATA AVAILABILITY STATEMENTS**

811 The data underlying this article are available in the article and in its online supplementary

812 material.

813 **REFERENCES**

814 Abramowitz, M., & Stegun, I. (1970). Dover. *Handbook of mathematical functions*.

815 Aki, K. (1965). Maximum likelihood estimate of b in the formula log N= a-bM and its

816   confidence limits. *Bull. Earthq. Res. Inst., Tokyo Univ.*, *43*, 237-239.

817 Amato, A., Azzara, R., Chiarabba, C., Cimini, G., Cocco, M., Di Bona, M., Margheriti, L.,

818   Mazza, S., Mele, F., & Selvaggi, G. (1998). The 1997 Umbria-Marche, Italy,

819   earthquake sequence : A first look at the main shocks and aftershocks. *Geophysical*

820   *Research Letters*, *25*(15), 2861-2864.

821 Antoine, S. L., Klinger, Y., Delorme, A., Wang, K., Bürgmann, R., & Gold, R. D. (2021).

822   Diffuse deformation and surface faulting distribution from submetric image

823   correlation along the 2019 Ridgecrest, California, ruptures. *Bull. Seismol. Soc. Am.*, *5*,

824   2275-2302.

825 Antonioli, A., Piccinini, D., Chiaraluce, L., & Cocco, M. (2005). Fluid flow and seismicity

826   pattern : Evidence from the 1997 Umbria-Marche (central Italy) seismic sequence.

827   *Geophysical Research Letters*, *32*(10).

828 Axen, G. J. (1992). Pore pressure, stress increase, and fault weakening in low-angle normal

829   faulting. *Journal of Geophysical Research*, *97*(B6), 8979.

830   https://doi.org/10.1029/92JB00517

831   Barberio, M. D., Barbieri, M., Billi, A., Doglioni, C., & Petitta, M. (2017). Hydrogeochemical

832   changes before and during the 2016 Amatrice-Norcia seismic sequence (central Italy).

833   *Scientific reports*, *7*(1), 1-12.

834   Barnhart, W. D., Hayes, G. P., & Gold, R. D. (2019). The July 2019 Ridgecrest, California

835   Earthquake Sequence : Kinematics of Slip and Stressing in Cross-Fault Ruptures.

836   *Geophysical Research Letters*, *0*(ja). https://doi.org/10.1029/2019GL084741

837   Berg, E. (1968). Relation between earthquake foreshocks, stress and mainshocks. *Nature*,

838   *219*(5159), 1141-1143.

839   Bird, P. (2017). Stress field models from Maxwell stress functions : Southern California.

840   *Geophysical Journal International*, *210*(2), 951-963.

841   https://doi.org/10.1093/gji/ggx207

842   Cappa, F., Scuderi, M. M., Collettini, C., Guglielmi, Y., & Avouac, J.-P. (2019). Stabilization

843   of fault slip by fluid injection in the laboratory and in situ. *Science advances*, *5*(3),

844   eaau4065.

845   Chambon, G., & Rudnicki, J. W. (2001). Effects of normal stress variations on frictional

846   stability of a fluid-infiltrated fault. *Journal of Geophysical Research: Solid Earth*,

847   *106*(B6), 11353-11372.

848   Cheloni, D., De Novellis, V., Albano, M., Antonioli, A., Anzidei, M., Atzori, S., Avallone,

849   A., Bignami, C., Bonano, M., Calcaterra, S., Castaldo, R., Casu, F., Cecere, G., De

850   Luca, C., Devoti, R., Di Bucci, D., Esposito, A., Galvani, A., Gambino, P., …

851   Doglioni, C. (2017). Geodetic model of the 2016 Central Italy earthquake sequence

852   inferred from InSAR and GPS data. *Geophysical Research Letters*, *44*(13),

853   6778-6787. https://doi.org/10.1002/2017GL073580

854   Chen, C.-T., Chan, Y.-C., Beyssac, O., Lu, C.-Y., Chen, Y.-G., Malavieille, J., Kidder, S. B.,

855   & Sun, H.-C. (2019). Thermal History of the Northern Taiwanese Slate Belt and

856   Implications for Wedge Growth During the Neogene Arc-Continent Collision.

857   *Tectonics*, *38*(9), 3335-3350. https://doi.org/10.1029/2019TC005604

858   Chiaraluce, L. (2012). Unravelling the complexity of Apenninic extensional fault systems : A

859   review of the 2009 L'Aquila earthquake (Central Apennines, Italy). *Journal of*

860   *Structural Geology*, *42*, 2-18.

861   Chiaraluce, L., Ellsworth, W., Chiarabba, C., & Cocco, M. (2003). Imaging the complexity of

862   an active normal fault system : The 1997 Colfiorito (central Italy) case study. *Journal*

863   *of Geophysical Research: Solid Earth*, *108*(B6).

864   Cocco, M., & Rice, J. R. (2002). Pore pressure and poroelasticity effects in Coulomb stress

865   analysis of earthquake interactions. *Journal of Geophysical Research: Solid Earth*,

866   *107*(B2), ESE-2.

867   Combs, J. (1980). Heat flow in the Coso Geothermal Area, Inyo County, California. *Journal*

868   *of Geophysical Research*, *85*(B5), 2411. https://doi.org/10.1029/JB085iB05p02411

869   Copley, A. (2018). The strength of earthquake-generating faults. *Journal of the Geological*

870   *Society*, *175*(1), 1-12. https://doi.org/10.1144/jgs2017-037

871   Dascher-Cousineau, K., Lay, T., & Brodsky, E. E. (2020). Two foreshock sequences post

872   Gulia and Wiemer (2019). *Seismological Society of America*, *91*(5), 2843-2850.

873   De Barros, L., Cappa, F., Deschamps, A., & Dublanchet, P. (2020). Imbricated aseismic slip

874   and fluid diffusion drive a seismic swarm in the Corinth Gulf, Greece. *Geophysical*

875   *Research Letters*, *47*(9), e2020GL087142.

876   Deschamps, A., Courboulex, F., Gaffet, S., Lomax, A., Virieux, J., Amato, A., Azzara, A.,

877   Castello, B., Chiarabba, C., & Cimini, G. (2000). Spatio-temporal distribution of

878   seismic activity during the Umbria-Marche crisis, 1997. *Journal of Seismology*, *4*(4),

879   377-386.

880   Enescu, B., Mori, J., & Miyazawa, M. (2007). Quantifying early aftershock activity of the

881   2004 mid-Niigata Prefecture earthquake (Mw6.6). *Journal of Geophysical Research:*

882   *Solid Earth*, *112*(B4). https://doi.org/10.1029/2006JB004629

883   Fielding, E. J., Liu, Z., Stephenson, O. L., Zhong, M., Liang, C., Moore, A., Yun, S., &

884   Simons, M. (2020). Surface Deformation Related to the 2019 M w 7.1 and 6.4

885   Ridgecrest Earthquakes in California from GPS, SAR Interferometry, and SAR Pixel

886   Offsets. *Seismological Research Letters*.

887   Gasperini, P., Lolli, B., & Vannucci, G. (2013). Empirical calibration of local magnitude data

888   sets versus moment magnitude in Italy. *Bulletin of the Seismological Society of*

889   *America*, *103*(4), 2227-2246.

890   Goebel, T. H. W., Schorlemmer, D., Becker, T. W., Dresen, G., & Sammis, C. G. (2013).

891   Acoustic emissions document stress changes over many seismic cycles in stick-slip

892   experiments. *Geophysical Research Letters*, *40*(10), 2049-2054.

893   https://doi.org/10.1002/grl.50507

894   Gulia, L., Tormann, T., Wiemer, S., Herrmann, M., & Seif, S. (2016). Short-term probabilistic

895   earthquake risk assessment considering time-dependent b values. *Geophysical*

896   *Research Letters*, *43*(3), 1100-1108. https://doi.org/10.1002/2015GL066686

897   Gulia, L., & Wiemer, S. (2019). Real-time discrimination of earthquake foreshocks and

898   aftershocks. *Nature*, *574*(7777), 193-199.

899   Gulia, L., Wiemer, S., & Vannucci, G. (2020). Pseudoprospective Evaluation of the

900   Foreshock Traffic-Light System in Ridgecrest and Implications for Aftershock Hazard

901   Assessment. *Seismological Society of America*, *91*(5), 2828-2842.

902   Guo, Z., & Ogata, Y. (1997). Statistical relations between the parameters of aftershocks in

903   time, space, and magnitude. *Journal of Geophysical Research: Solid Earth*, *102*(B2),

904   2857-2873.

905   Gutenberg, G., & Richter, C. (1950). Seismicity of the earth and associated phenomena,

906   Howard Tatel. *JGR*, *55*, 97.

907   Hauksson, E. (2015). Average Stress Drops of Southern California Earthquakes in the Context

908   of Crustal Geophysics : Implications for Fault Zone Healing. *Pure and Applied*

909   *Geophysics*, *172*(5), 1359-1370. https://doi.org/10.1007/s00024-014-0934-4

910   Hauksson, E., Hutton, K., Kanamori, H., Jones, L., Mori, J., Hough, S., & Roquemore, G.

911   (1995). Preliminary Report on the 1995 Ridgecrest Earthquake Sequence in Eastern

912   California. *Seismological Research Letters*, *66*(6), 54-60.

913   https://doi.org/10.1785/gssrl.66.6.54

914   Hirakawa, E., & Barbour, A. J. (2020). Kinematic Rupture and 3D Wave Propagation

915   Simulations of the 2019 Mw 7.1 Ridgecrest, California, Earthquake. *Bulletin of the*

916   *Seismological Society of America*, *110*(4), 1644-1659.

917   https://doi.org/10.1785/0120200031

918   Hudnut, K. W., Seeber, L., & Pacheco, J. (1989a). Cross-fault triggering in the November

919   1987 Superstition Hills earthquake sequence, southern California. *Geophysical*

920   *Research Letters*, *16*(2), 199-202.

921   Kanamori, H. (1994). MECHANICS OF EARTHQUAKES. *Annual Review of Earth and*

922   *Planetary Sciences*, *22*(1), 207-237.

923   https://doi.org/10.1146/annurev.ea.22.050194.001231

924   Kariche, J. (2022). The 2020 Monte Cristo (Nevada) Earthquake Sequence : Stress Transfer in

925   the Context of Conjugate Strike-Slip Faults. *Tectonics*, *41*(3), e2020TC006506.

926   Kariche, J., Meghraoui, M., Timoulali, Y., Cetin, E., & Toussaint, R. (2018). The Al Hoceima

927   earthquake sequence of 1994, 2004 and 2016 : Stress transfer and poroelasticity in the

928   Rif and Alboran Sea region. *Geophysical Journal International*, *212*(1), 42-53.

929   https://doi.org/10.1093/gji/ggx385

930   Khoshmanesh, M., & Shirzaei, M. (2018). Episodic creep events on the San Andreas Fault

931   caused by pore pressure variations. *Nature geoscience*, *11*(8), 610.

932   Lozos, J. C., & Harris, R. A. (2020). Dynamic Rupture Simulations of the *M* 6.4 and *M* 7.1

933   July 2019 Ridgecrest, California, Earthquakes. *Geophysical Research Letters*, *47*(7).

934   https://doi.org/10.1029/2019GL086020

935   Main, I. G., Meredith, P. G., Sammonds, P. R., & Jones, C. (1990). Influence of fractal flaw

936   distributions on rock deformation in the brittle field. *Geological Society, London,*

937   *Special Publications*, *54*(1), 81-96.

938   Malagnini, L., Lucente, F. P., De Gori, P., Akinci, A., & Munafo', I. (2012). Control of pore

939   fluid pressure diffusion on fault failure mode : Insights from the 2009 L'Aquila

940   seismic sequence. *Journal of Geophysical Research: Solid Earth*, *117*(B5).

941   Miller, S. A. (2020). Aftershocks are fluid-driven and decay rates controlled by permeability

942   dynamics. *Nature communications*, *11*(1), 1-11.

943   Monastero, F. C., Walker, J. D., Katzenstein, A. M., Sabin, A. E., Glazner, A., & Bartley, J.

944   (2002). Neogene evolution of the Indian Wells Valley, east-central California.

945   *Geologic evolution of the Mojave Desert and southwestern Basin and Range:*

946   *Geological Society of America Memoir*, *195*, 199-228.

947   Moro, M., Saroli, M., Stramondo, S., Bignami, C., Albano, M., Falcucci, E., Gori, S.,

948   Doglioni, C., Polcari, M., & Tallini, M. (2017). New insights into earthquake

949   precursors from InSAR. *Scientific reports*, *7*(1), 12035.

950   Nanjo, K., Hirata, N., Obara, K., & Kasahara, K. (2012). Decade-scale decrease inb value

951   prior to the M9-class 2011 Tohoku and 2004 Sumatra quakes. *Geophysical Research*

952   *Letters*, *39*(20).

953 Nespoli, M., Belardinelli, M. E., Gualandi, A., Serpelloni, E., & Bonafede, M. (2018).

954   Poroelasticity and Fluid Flow Modeling for the 2012 Emilia-Romagna Earthquakes :

955   Hints from GPS and InSAR Data. *Geofluids*, *2018*.

956 Nur, A. (1972). Dilatancy, pore fluids, and premonitory variations of ts/tp travel times.

957   *Bulletin of the Seismological society of America*, *62*(5), 1217-1222.

958 Nur, A., & Booker, J. R. (1972). Aftershocks caused by pore fluid flow? *Science*, *175*(4024),

959   885-887.

960 Ogata, Y., & Omi, T. (2020). Statistical Monitoring and Early Forecasting of the Earthquake

961   Sequence : Case Studies after the 2019 M 6.4 Searles Valley Earthquake, California.

962   *Bulletin of the Seismological Society of America*.

963 Pino, N. A., Convertito, V., & Madariaga, R. (2019). Clock advance and magnitude limitation

964   through fault interaction : The case of the 2016 central Italy earthquake sequence.

965   *Scientific reports*, *9*(1), 5005.

966 Pio Lucente, F., De Gori, P., Margheriti, L., Piccinini, D., Di Bona, M., Chiarabba, C., &

967   Piana Agostinetti, N. (2010). Temporal variation of seismic velocity and anisotropy

968   before the 2009 MW 6.3 L'Aquila earthquake, Italy. *Geology*, *38*(11), 1015-1018.

969 Proctor, B., Lockner, D., Kilgore, B., Mitchell, T., & Beeler, N. (2020). Direct evidence for

970   fluid pressure, dilatancy, and compaction affecting slip in isolated faults. *Geophysical*

971   *Research Letters*, *47*(16), e2019GL086767.

972 Rice, J. R. (1992). Chapter 20 Fault Stress States, Pore Pressure Distributions, and the

973   Weakness of the San Andreas Fault. In *International Geophysics* (Vol. 51, p.

974   475-503). Elsevier. https://doi.org/10.1016/S0074-6142(08)62835-1

975 Rikitake, T. (1972). Earthquake prediction studies in Japan. *Geophysical surveys*, *1*(1), 4-26.

976 Ross, Z. E., Trugman, D. T., Hauksson, E., & Shearer, P. M. (2019). Searching for hidden

977   earthquakes in Southern California. *Science*, *364*(6442), 767-771.

978   Ruhl, C., Abercrombie, R., Smith, K., & Zaliapin, I. (2016). Complex spatiotemporal

979   evolution of the 2008 Mw 4.9 Mogul earthquake swarm (Reno, Nevada) : Interplay of

980   fluid and faulting. *Journal of Geophysical Research: Solid Earth*, *121*(11), 8196-8216.

981   Sammonds, P., Meredith, P., & Main, I. (1992). Role of pore fluids in the generation of

982   seismic precursors to shear fracture. *Nature*, *359*(6392), 228-230.

983   Scholz, C. H. (1968). The frequency-magnitude relation of microfracturing in rock and its

984   relation to earthquakes. *Bulletin of the Seismological Society of America*, *58*(1),

985   399-415. https://doi.org/10.1785/BSSA0580010399

986   Scholz, C. H. (2015). On the stress dependence of the earthquake b value. *Geophysical*

987   *Research Letters*, *42*(5), 1399-1402.

988   Scholz, C. H. (2019). *The mechanics of earthquakes and faulting*. Cambridge university press.

989   Scholz, C. H., Sykes, L. R., & Aggarwal, Y. P. (1973). Earthquake prediction : A physical

990   basis. *Science*, *181*(4102), 803-810.

991   Scholz, C., & Kranz, R. (1974). Notes on dilatancy recovery. *Journal of Geophysical*

992   *Research*, *79*(14), 2132-2135.

993   Segall, P., & Rice, J. R. (1995). Dilatancy, compaction, and slip instability of a fluid-

994   infiltrated fault. *Journal of Geophysical Research: Solid Earth*, *100*(B11),

995   22155-22171.

996   Shearer, P. M., Prieto, G. A., & Hauksson, E. (2006). Comprehensive analysis of earthquake

997   source spectra in southern California : SOUTHERN CALIFORNIA SOURCE

998   SPECTRA. *Journal of Geophysical Research: Solid Earth*, *111*(B6), n/a-n/a.

999   https://doi.org/10.1029/2005JB003979

1000   Shelly, D. R. (2020). A high-resolution seismic catalog for the initial 2019 Ridgecrest

1001   earthquake sequence : Foreshocks, aftershocks, and faulting complexity.

1002   *Seismological Research Letters*.

1003   Sheng, S., & Meng, L. (2020). Stress Field Variation During the 2019 Ridgecrest Earthquake

1004   Sequence. *Geophysical Research Letters*, *47*(15), e2020GL087722.

1005   Shi, Y., & Bolt, B. A. (1982). The standard error of the magnitude-frequency b value. *Bulletin*

1006   *of the Seismological Society of America*, *72*(5), 1677-1687.

1007   Smith, W. D. (1981). The b-value as an earthquake precursor. *Nature*, *289*(5794), 136-139.

1008   Soldati, G., Zaccarelli, L., & Faenza, L. (2019). Spatio-temporal seismic velocity variations

1009   associated to the 2016–2017 central Italy seismic sequence from noise cross-

1010   correlation. *Geophysical Journal International*, *219*(3), 2165-2173.

1011   Stramondo, S., Tesauro, M., Briole, P., Sansosti, E., Salvi, S., Lanari, R., Anzidei, M., Baldi,

1012   P., Fornaro, G., & Avallone, A. (1999). The September 26, 1997 Colfiorito, Italy,

1013   earthquakes : Modeled coseismic surface displacement from SAR interferometry and

1014   GPS. *Geophysical research letters*, *26*(7), 883-886.

1015   Tan, Y. J., Waldhauser, F., Ellsworth, W. L., Zhang, M., Zhu, W., Michele, M., Chiaraluce,

1016   L., Beroza, G. C., & Segou, M. (2021). Machine-learning-based high-resolution

1017   earthquake catalog reveals how complex fault structures were activated during the

1018   2016–2017 Central Italy sequence. *The Seismic Record*, *1*(1), 11-19.

1019   Tong, P., Yao, J., Liu, Q., Li, T., Wang, K., Liu, S., Cheng, Y., & Wu, S. (2021). Crustal

1020   rotation and fluids : Factors for the 2019 Ridgecrest earthquake sequence?

1021   *Geophysical Research Letters*, *48*(3), e2020GL090853.

1022   Tormann, T., Wiemer, S., Metzger, S., Michael, A., & Hardebeck, J. L. (2013). Size

1023   distribution of Parkfield's microearthquakes reflects changes in surface creep rate.

1024   *Geophysical Journal International*, *193*(3), 1474-1478.

1025   https://doi.org/10.1093/gji/ggt093

1026   Trugman, D. T. (2020). Stress-Drop and Source Scaling of the 2019 Ridgecrest, California,

1027   Earthquake Sequence. *Bulletin of the Seismological Society of America*.

1028   Utsu, T., & Ogata, Y. (1995). The centenary of the Omori formula for a decay law of

1029   aftershock activity. *Journal of Physics of the Earth*, *43*(1), 1-33.

1030   Wang, K., & Bürgmann, R. (2020). Co- and Early Postseismic Deformation Due to the 2019

1031   Ridgecrest Earthquake Sequence Constrained by Sentinel-1 and COSMO-SkyMed

1032   SAR Data. *Seismological Research Letters*. https://doi.org/10.1785/0220190299

1033   Wiemer, S. (2001). A software package to analyze seismicity : ZMAP. *Seismological*

1034   *Research Letters*, *72*(3), 373-382.

1035   Wiemer, S., & Wyss, M. (2000). Minimum magnitude of completeness in earthquake

1036   catalogs : Examples from Alaska, the western United States, and Japan. *Bulletin of the*

1037   *Seismological Society of America*, *90*(4), 859-869.

1038   Woessner, J., & Wiemer, S. (2005). Assessing the quality of earthquake catalogues :

1039   Estimating the magnitude of completeness and its uncertainty. *Bulletin of the*

1040   *Seismological Society of America*, *95*(2), 684-698.

1041   Wyss, M., & Habermann, R. E. (1988). Precursory seismic quiescence. *Pure and Applied*

1042   *Geophysics*, *126*(2), 319-332.

1043   Wyss, M., & McNutt, S. R. (1998). Temporal and three-dimensional spatial analyses of the

1044   frequency–magnitude distribution near Long Valley Caldera, California. *Geophysical*

1045   *Journal International*, *134*(2), 409-421.

1046   Wyss, M., & Wiemer, S. (2000). Change in the probability for earthquakes in southern

1047   California due to the Landers magnitude 7.3 earthquake. *Science*, *290*(5495),

1048   1334-1338.

1049   Xu, X., Sandwell, D. T., & Smith-Konter, B. (2020). Coseismic Displacements and Surface

1050   Fractures from Sentinel-1 InSAR : 2019 Ridgecrest Earthquakes. *Seismological*

1051   *Research Letters*. https://doi.org/10.1785/0220190275

1052

Role of fluid on earthquake occurrence: Example of the 2019 Ridgecrest and the 1997-2016 Central Apennines sequences

by J.Kariche

List of Figure Captions

Figure S1

Seismotectonic map of the southern Walker Lane including the 1872 Owens Valley earthquake and its major aftershocks. The 1872 Owens Valley focal mechanism solutions and locations are from Deng & Sykes. (1997). The fault ruptures trace associated with the 1872 Owens Valley earthquake is represented by thick lines. The focal solutions of the Mw 6.4 and Mw 7.1 Ridgecrest earthquakes are from USGS-NEIC. The fault trace related to the 2019 Ridgecrest sequence (thick lines) is from Ross et al. (2019). The Quaternary active faults associated with the Walker Lane domain and ECSZ are from the USGS database (https://earthquake.usgs.gov/hazards/qfaults/, last updated in 2017).

Figure S2

Seismicity analysis along the central Apennines spanning the period from 1985 to 01/01/2009

A) Map of seismicity centered on the 1997 Colfiorito earthquake sequences. The yellow stars represent the location of major events with Mw>5.0. The blue lines represent the location of major actives faults in central Italy obtained from the EDSF project (Basili et al., 2013). The green lines represent the surface projection of the Colfiori faults plane (based on the rupture model of Hernandez et al.(2004). The purple lines represent the updated actives faults for

Central Apennines extracted from the Fault2SHA project (Scotti et al., 2021). **B)** Depth through time cross-section for a period between 1985 to pre-L'Aquila mainshock.

C) Cross-section along rectangular volume (in red in Figure S1A) oriented NW-SE. The yellows stars are major earthquakes related to the 1997 Colfiorito sequence as shown in the paper (figure 1). Note that the selected events for Cross-section in B) and C) are the earthquakes inside the Cross-section CC'.

Figure S3

Seismicity analysis along the central Apennines covering the period from 01/01/2009 to 01/05/2009.

A) Map of seismic events related to the 06/04/2009 (Mw 6.3) L'Aquila sequence. The black rectangles represent plotted seismicity start on January 1, 2009 and finish just before the Mw6.3 L'Aquila mainshocks. The grey rectangles represent the aftershocks activity following the Mw6.3 2009 L'Aquila earthquake and cut on June14, 2009. The yellow stars represent the location of the L'Aquila mainshock. **B)** Frequency Magnitude Distribution FMD in the ~ 3 months before the L'Aquila earthquake. The b and Mc values are obtained by a maximum curvature estimate (Wiemer & Wyss, 2000). **C)** Time–depth cross-section of ~3-month seismicity before the L'Aquila mainshock.

Figure S4

Seismicity analysis following the 2016 (Mw6.5) Norcia sequence.

A) Aftershock distribution related to the Mw6.5 30/10/2016 Norcia earthquake. The yellow star represents the location of the mainshock, the grey star represents the location of the 24/08/2016 Amatrice Foreshock. **B)** Cumulative events time series in the Norcia basin spanning

the period from 1985 to 2017. **C)** FMD associated with the 2016 Norcia earthquake sequence, uncertainties are obtained by maximum curvature estimate <u>(Wiemer & Wyss, 2000).</u>

Figure S5

Seismicity analysis in Southern California.

A) Spatial distribution of seismicity in ECSZ spanning the period from 2000 to 2019. **B)** Cumulative earthquakes time series plot in ECSZ from periods range from 2000 to 2019, the yellow stars represent the time location of the Mw6.4 Foreshock and the Mw7.1 mainshock. **C)** FMD for the 2019 Ridgecrest earthquake sequence. The Magnitude of completeness is obtained using the maximum likelihood approach. The G-R values (a and b) are obtained using the maximum curvature estimate. The earthquake catalog using for this supplemental material is the same as in the main article.

<u>**Figure S6**</u>

<u>Time evolution of the number of earthquakes from 2000 to August 2019 associated to a</u> <u>seismogenic volume around the Ridgecrest fault zone through each point of the b-value time</u> <u>series. The b-value time series was performed using time windows with selected earthquakes</u> <u>with radius R~ 30 km centered at coordinate = (-117,7243°, 35.7031°). The calculation</u> <u>method is based on the Maximum curvature approach with sample windows size = 250 events</u> <u>and windows overlap of 4%.</u>

<u>**Figure S7**</u>

<u>Time evolution of the number of earthquakes from 2007 to August 2017 associated to the</u> <u>central Appennines fault zone through each point of the b-value time series. The calculation</u> <u>method is the same as in the Figure S6.</u>

<u>**Figure S8**</u>

Comparison of b-value time-series for various constant number of event N associated to the 2016 Amatrice earthquake sequence. The sampling technique is based on using a moving windows approach of a fixed number of N events. This approach gives a robust estimate from different lengths of time windows. The b-value time series show that the shape of time series is preserved for $100 \leq N \leq 500$.
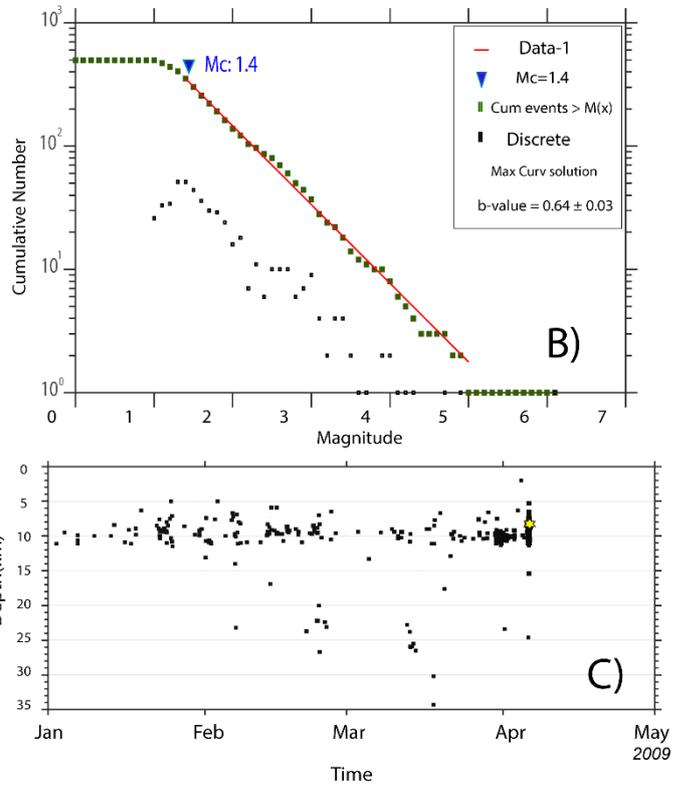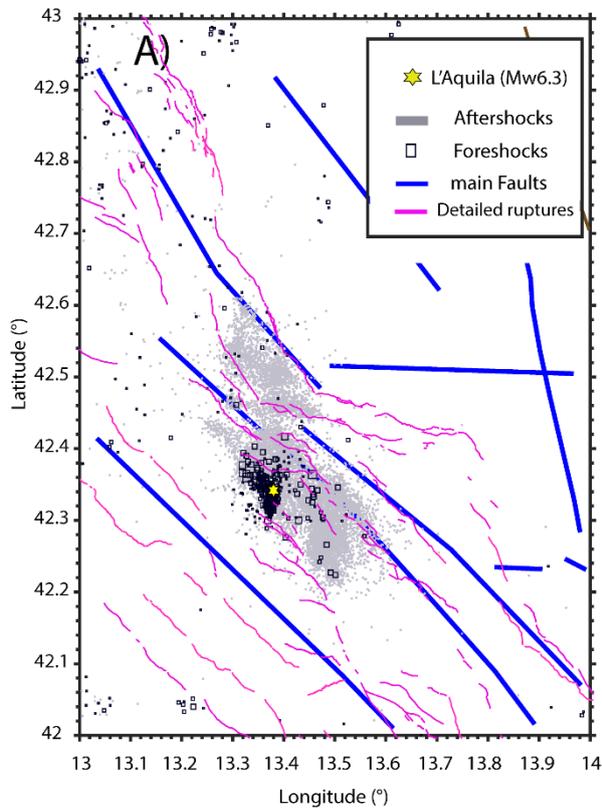
Figure S9

Comparison of b-value time-series for various constant number of event N associated to the 2019 Ridgecrest earthquake sequence. The sampling technique is the same as in figure S9. As for the Amatrice case, the b-value time series show that the shape of time series is preserved for $100 \leq N \leq 500$.

Figure S10

Geographical footprint related to the selected earthquake (datasets on the polygon) and used to construct Figure 7 of the manuscript. As for Figure 7, the catalog used here is defined as the combination of the INGV and the Gasperini et al. (2013) catalogs. For all Figures, the seismicity analysis is made using the Zmap 7 software (Reyes & Wiemer, 2020).

03/04/1872
(Mℓ 6.1)

26/03/1872
(Mℓ 6.5)

O.V.F.Z

26/03/1872
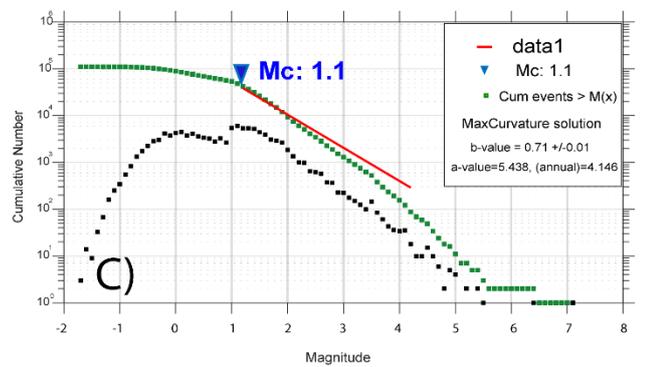(Mw7.8)

06/07/2019
(Mw7.1)

R.F.Z
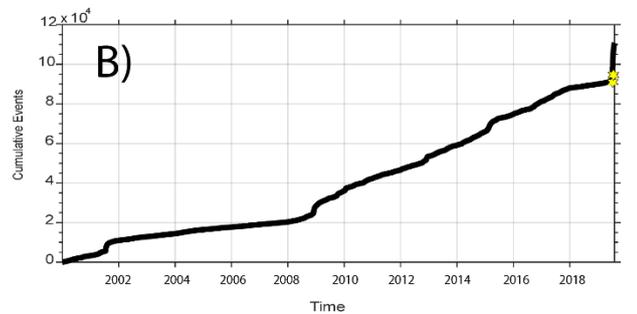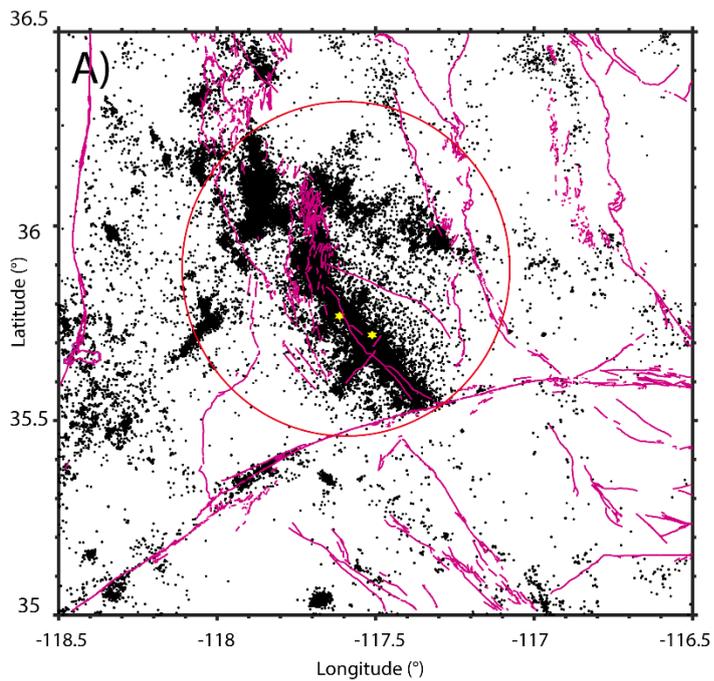
04/07/2019
(Mw6.4)

38.5°

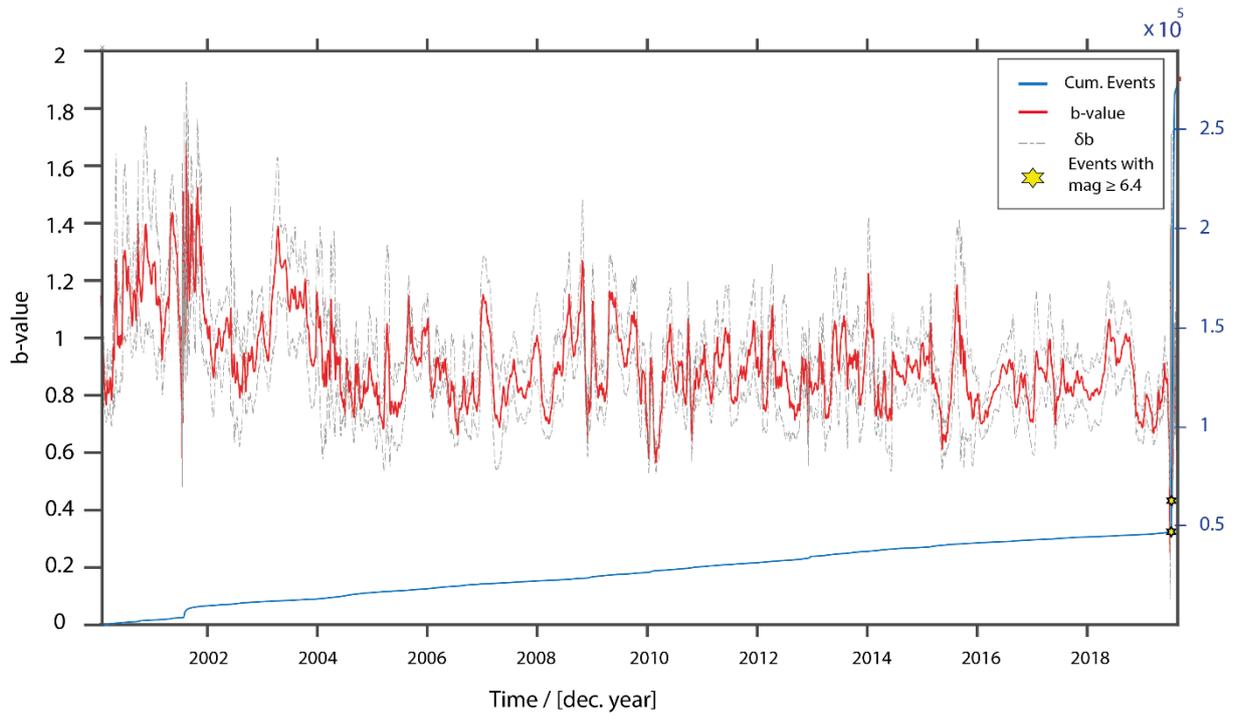36°

35°

-118.4°

-116.6°
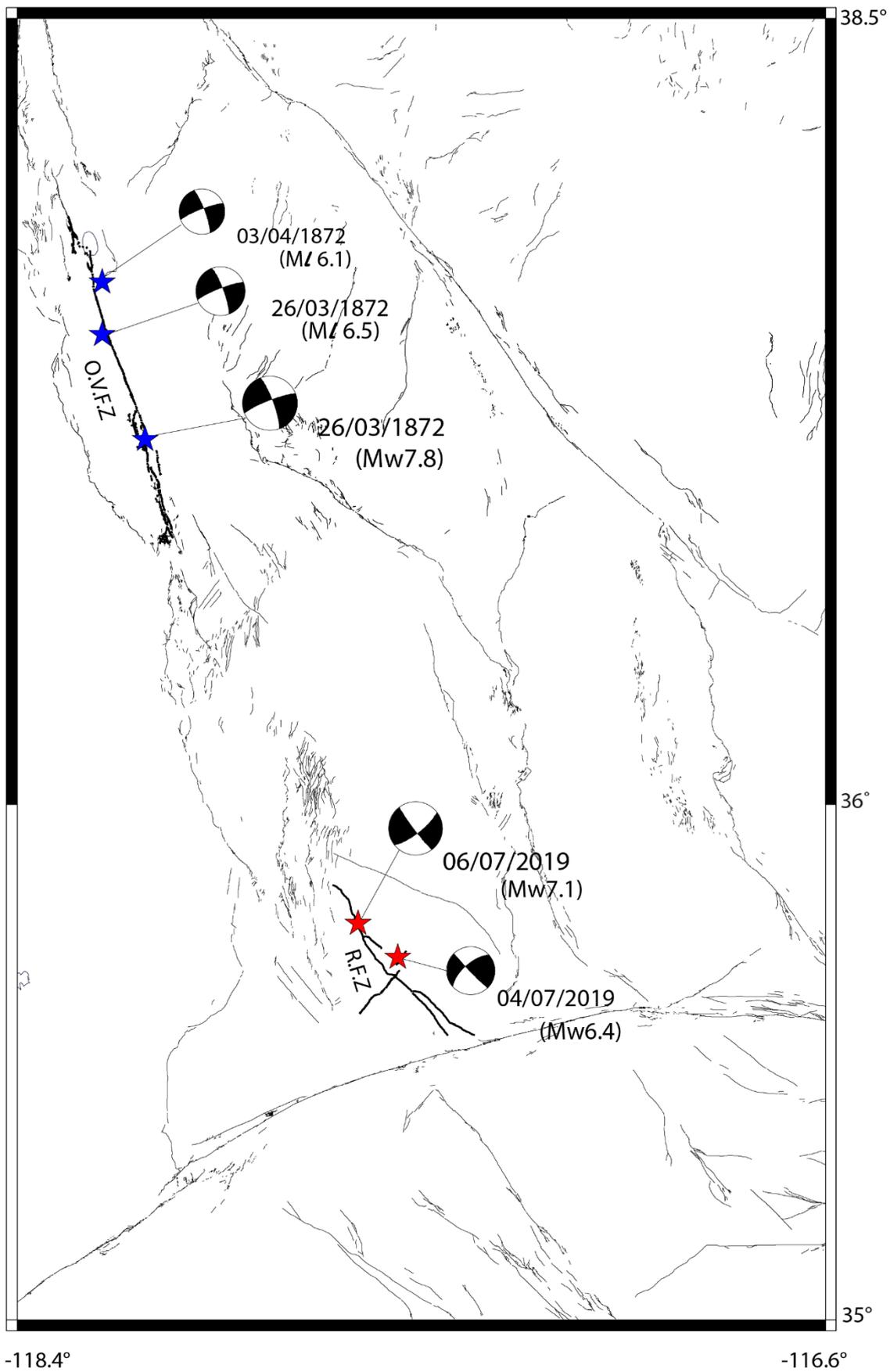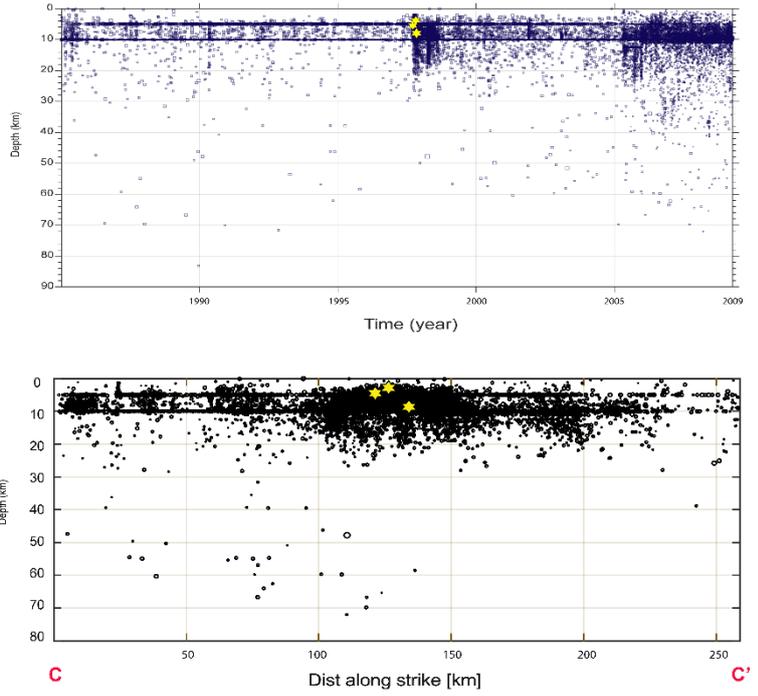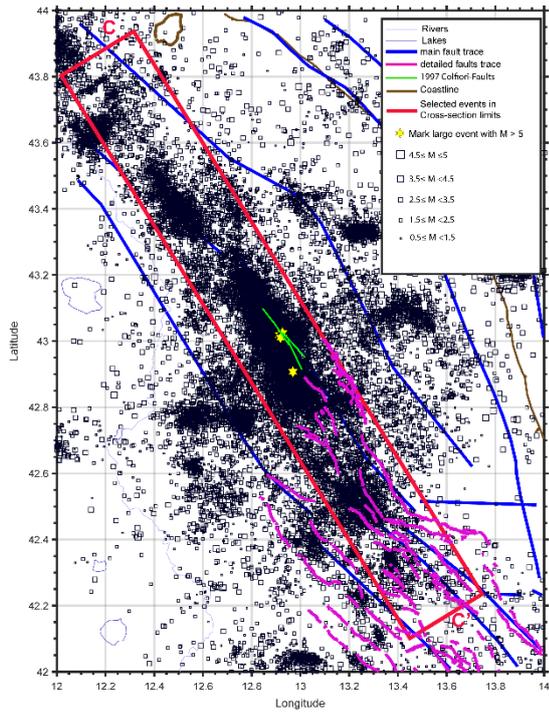
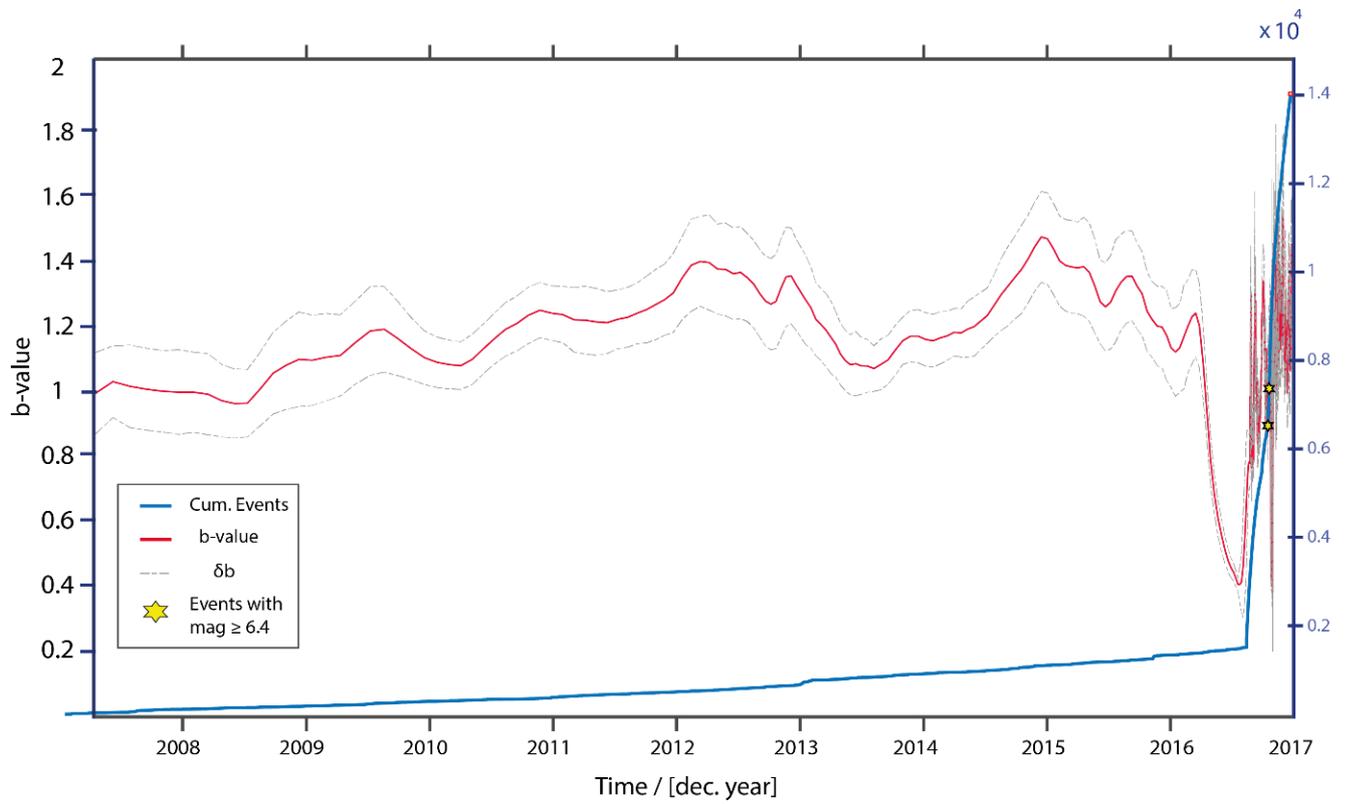**Figure S1**

Figure S2

Figure S3
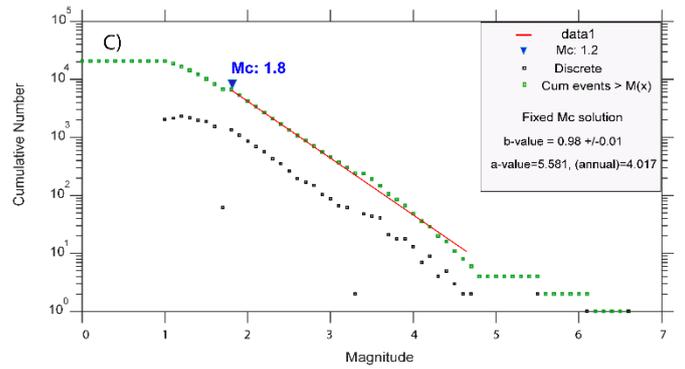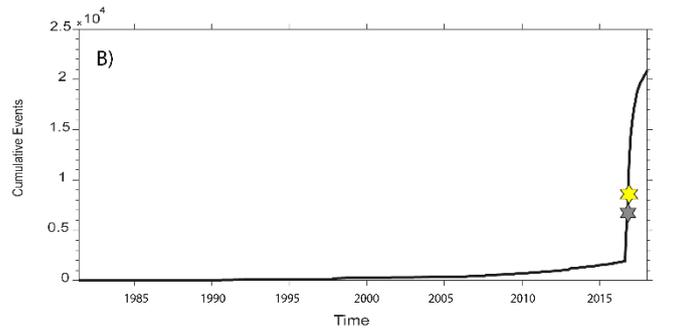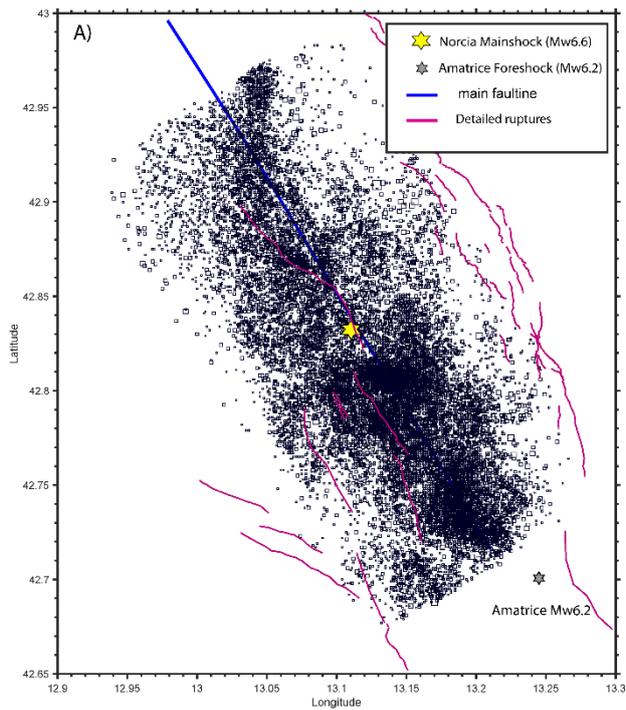
 Figure S4
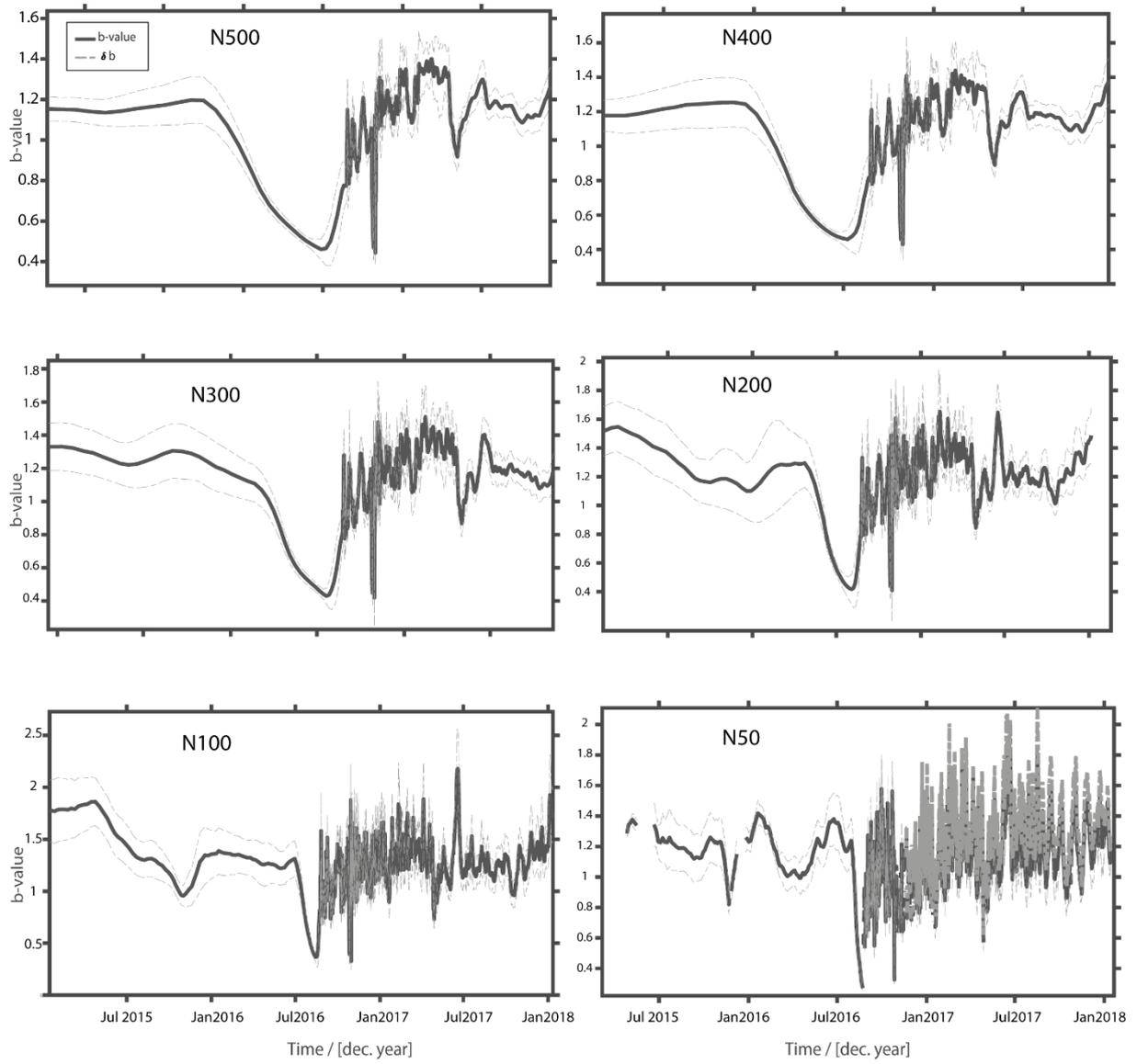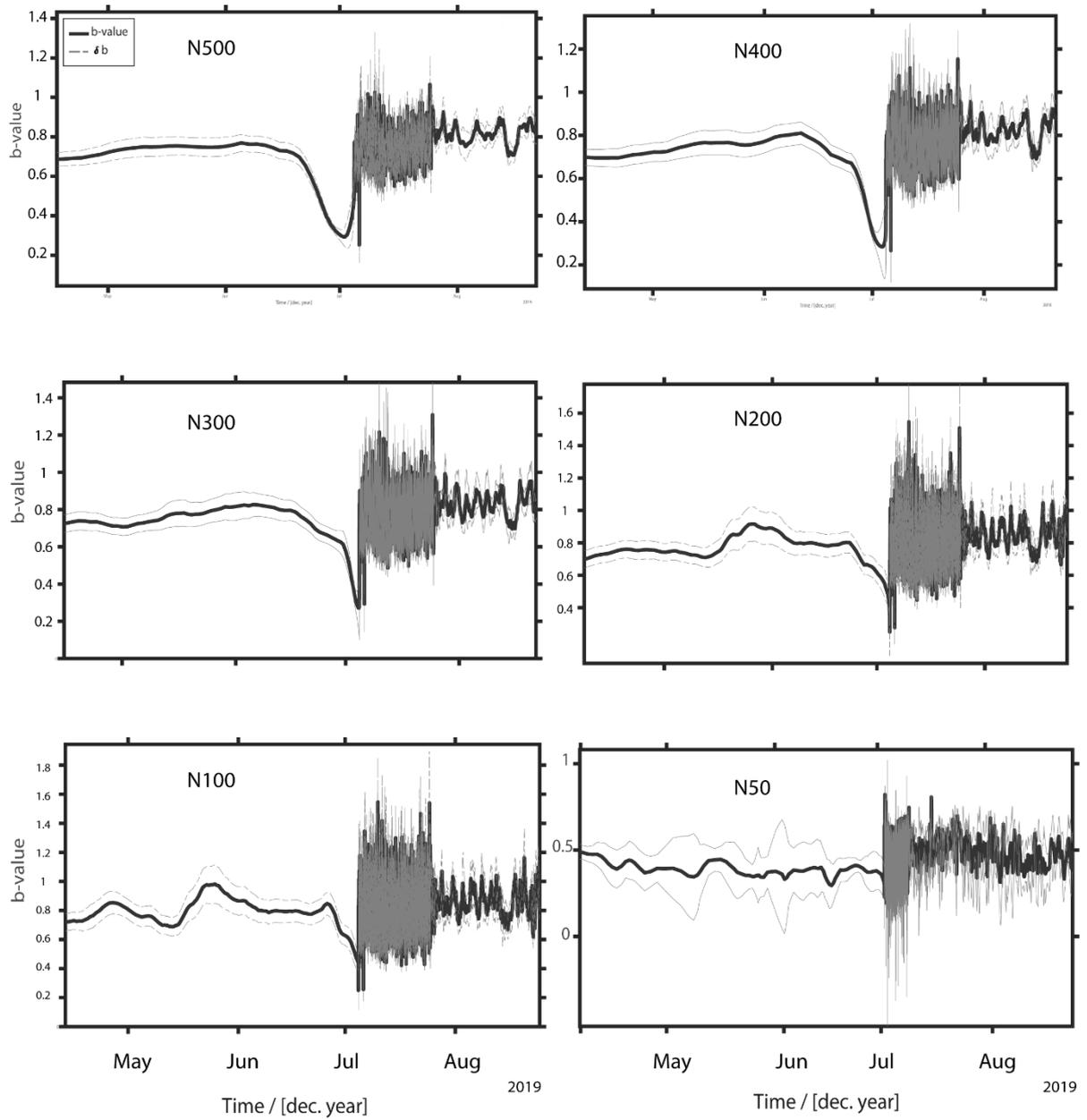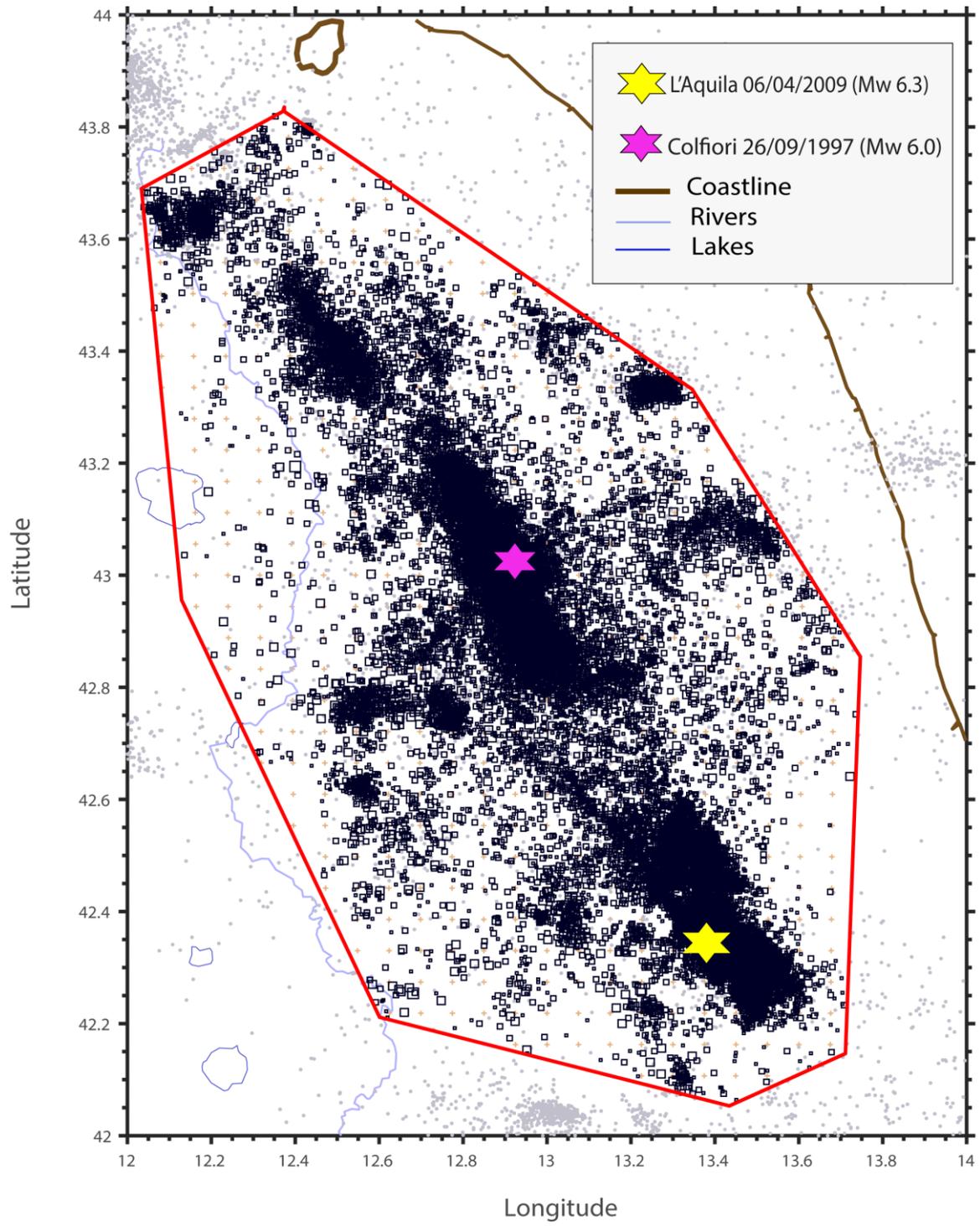

Figure S5

Figure S6

Figure S7

Figure S8

Figure S9

Figure S10

References

Basili, R., Kastelic, V., Demircioglu, M. B., Garcia Moreno, D., Nemser, E. S., Petricca, P., Sboras, S. P., Besana-Ostman, G. M., Cabral, J., Camelbeeck, T., Caputo, R., Danciu, L., Domaç, H., Fonseca, J. F. de B. D., García-Mayordomo, J., Giardini, D., Glavatovic, B., Gulen, L., Ince, Y., … Wössner, J. (2013). *European Database of Seismogenic Faults (EDSF)* (p. 1131 fault sources) [Text/html,application/vnd.google-earth.kml+xml,application/vnd.mif,application/x-zipped-shp]. Istituto Nazionale di Geofisica e Vulcanologia (INGV). https://doi.org/10.6092/INGV.IT-SHARE-EDSF

Deng, J., & Sykes, L. R. (1997). Evolution of the stress field in southern California and triggering of moderate-size earthquakes: A 200-year perspective. *Journal of Geophysical Research: Solid Earth*, *102*(B5), 9859-9886.

Gasperini, P., Lolli, B., & Vannucci, G. (2013). Empirical calibration of local magnitude data sets versus moment magnitude in Italy. *Bulletin of the Seismological Society of America*, *103*(4), 2227-2246.

Hernandez, B., Cocco, M., Cotton, F., Stramondo, S., Scotti, O., Courboulex, F., & Campillo, M. (2004). Rupture history of the 1997 Umbria-Marche (Central Italy) main shocks from the inversion of GPS, DInSAR and near field strong motion data. *Annals of Geophysics*, *47*(4).

Reyes, C., & Wiemer, S. (2020). *From ZMAP to ZMAP7 : Fast-forwarding 25 years of software evolution*. 18878.

Ross, Z. E., Idini, B., Jia, Z., Stephenson, O. L., Zhong, M., Wang, X., Zhan, Z., Simons, M., Fielding, E. J., & Yun, S.-H. (2019). Hierarchical interlocked orthogonal faulting in the 2019 Ridgecrest earthquake sequence. *Science*, *366*(6463), 346-351.

Scotti, O., Visini, F., Faure Walker, J., Peruzza, L., Pace, B., Benedetti, L., Boncio, P., & Roberts, G. (2021). Which fault threatens me most ? Bridging the gap between

geologic data-providers and seismic risk practitioners. *Frontiers in Earth Science*, *8*, 626401.

Wiemer, S., & Wyss, M. (2000). Minimum magnitude of completeness in earthquake catalogs : Examples from Alaska, the western United States, and Japan. *Bulletin of the Seismological Society of America*, *90*(4), 859-869.